The Astrophysical Journal Supplement Series, 216:9 (34pp), 2015 January doi:10.1088/0067-0049/216/1/9


# INTEGRAL-FIELD STELLAR AND IONIZED GAS KINEMATICS OF PECULIAR VIRGO CLUSTER SPIRAL GALAXIES

Juan R. Cortés[1,2,3,5], Jeffrey D. P. Kenney[4], and Eduardo Hardy[1,3,5,6]
[1] National Radio Astronomy Observatory Avenida Nueva Costanera 4091, Vitacura, Santiago, Chile; jcortes@alma.cl, ehardy@nrao.cl
[2] Joint ALMA Observatory Alonso de Córdova 3107, Vitacura, Santiago, Chile
[3] Departamento de Astronomía, Universidad de Chile Casilla 36-D, Santiago, Chile
[4] Department of Astronomy, Yale University, P.O. Box 208101, New Haven, CT 06520-8101, USA; jeff.kenney@yale.edu
*Received 2014 March 10; accepted 2014 November 7; published 2014 December 24*

## ABSTRACT

We present the stellar and ionized gas kinematics of 13 bright peculiar Virgo cluster galaxies observed with the DensePak Integral Field Unit at the WIYN 3.5 m telescope in order to look for kinematic evidence that these galaxies have experienced gravitational interactions or gas stripping. Two-dimensional maps of the stellar velocity $V$, stellar velocity dispersion $\sigma$, and the ionized gas velocity (H$\beta$ and/or [O III]) are presented for the galaxies in the sample. The stellar rotation curves and velocity dispersion profiles are determined for 13 galaxies, and the ionized gas rotation curves are determined for 6 galaxies. Misalignments between the optical and kinematical major axes are found in several galaxies. While in some cases this is due to a bar, in other cases it seems to be associated with gravitational interaction or ongoing ram pressure stripping. Non-circular gas motions are found in nine galaxies, with various causes including bars, nuclear outflows, or gravitational disturbances. Several galaxies have signatures of kinematically distinct stellar components, which are likely signatures of accretion or mergers. For all of our galaxies, we compute the angular momentum parameter $\lambda_R$. An evaluation of the galaxies in the $\lambda_R$ ellipticity plane shows that all but two of the galaxies have significant support from random stellar motions, and have likely experienced gravitational interactions. This includes some galaxies with very small bulges and truncated/compact H$\alpha$ morphologies, indicating that such galaxies cannot be fully explained by simple ram pressure stripping, but must have had significant gravitational encounters. Most of the sample galaxies show evidence for ICM-ISM stripping as well as gravitational interactions, indicating that the evolution of a significant fraction of cluster galaxies is likely strongly impacted by both effects.

*Key words:* galaxies: evolution – galaxies: interactions – galaxies: ISM – galaxies: kinematics and dynamics – galaxies: nuclei – galaxies: peculiar

## 1. INTRODUCTION

It is well known that the environment affects the morphological types of galaxies in clusters. Many studies have shown that galaxies in clusters evolve morphologically with spirals becoming redder and in some cases lenticular as the result of environmental effects (Dressler 1980; Butcher & Oemler 1978, 1984; Dressler et al. 1997; Poggianti et al. 1999, 2009; Kormendy & Bender 2012) Several mechanisms have been proposed for driving galaxy evolution, including processes that affect the stars, gas, and dark matter, and processes that affect only the gas. In the first category, we include the following: (1) low-velocity tidal interactions and mergers (e.g., Toomre & Toomre 1972; Hernquist 1992), (2) high-velocity tidal interactions and collisions (e.g., Moore et al. 1996), and (3) tidal interaction between galaxies and the cluster as a whole or between galaxies and substructures within the cluster (Bekki 1999). In the second category, we include the following: (1) intracluster medium–interstellar medium (ICM-ISM) stripping (Gunn & Gott 1972; Nulsen 1982; Schulz & Struck 2001; Vollmer et al. 2001; van Gorkom 2004; Cen 2014), (2) gas accretion, which may occur in the outskirt of clusters, and (3) starvation or strangulation, where the galaxies could lose their gas reservoir, thus preventing their accretion onto the galaxy (Larson et al. 1980). While all of these processes probably do actually occur, it remains unclear which ones are dominant in driving the morphological evolution of cluster galaxies.

Detailed studies of stellar and ionized gas kinematics can help to discriminate between the different interaction processes. For example, gravitational interactions produce disturbed kinematics in both the stellar and gas components, whereas interactions of a hydrodynamic nature will directly affect only the gas. Recently, with the advent of Integral Field Units (IFUs) such as DensePak, SAURON, GMOS, SINFONI, and MUSE, these detailed studies have become possible. The observed velocity fields can be compared with those from simulations (e.g., Bendo & Barnes 2000; Jesseit et al. 2007; Kronberger et al. 2007, 2008), providing important clues about the physical processes that drive galaxy evolution.

The Virgo cluster is the nearest moderately rich cluster with a galaxy population spanning a large range of morphological types. The cluster has a moderately dense ICM and is dynamically young with on-going sub-cluster mergers and infalling galaxies, making it an ideal place for detailed studies of various environmental processes. Moreover, the Virgo cluster has a significant population of galaxies characterized by truncated star formation morphologies with no H$\alpha$ in the outer disk but strong H$\alpha$ in the inner region (Koopmann & Kenney, 2004), consistent with ICM-ISM stripping. However, some of them also have other peculiarities that are not presently well understood, presumably reflecting different types of interactions. These peculiar

[5] The National Radio Astronomy Observatory is a facility of the National Science Foundation operated under cooperative agreement by Associated Universities, Inc.
[6] Adjoint Professor.

**Table 1**
Galaxy Sample Properties

| Name (1) | R.A. (J2000) (2) | Decl. (J200) (3) | RSA/BST (4) | RC3 (5) | $C_{30}$ (6) | SFC (7) | $H_c$ (8) | $M_H$ (9) | $R_{25}$ (arcsec) (10) | Inc. (deg) (11) | PA (deg) (12) | $V_{\rm helio}$ (km s$^{-1}$) (13) | $D_{M87}$ (deg) (14) | $D$ (Mpc) (15) |
|---|---|---|---|---|---|---|---|---|---|---|---|---|---|---|
| NGC 4064 | 12 04 11.2 | 18 26 36 | SBc(s): | SB(s)a:pec | 0.43 | T/C | 8.78[a] | $-22.5 \pm ^{0.1}_{0.2}$ | 138 | 70 | 148 | 931 ± 12 | 8.8 | $18.0 \pm ^{1.3}_{0.8}$ |
| NGC 4293 | 12 21 12.8 | 18 22 57 | Sa pec | (R)SB(s)0/a | 0.40 | T/A | 7.35 | $-23.4 \pm ^{0.3}_{0.2}$ | 216 | 67 | 62 | 930 ± 14 | 6.4 | $14.1 \pm ^{1.0}_{1.5}$ |
| NGC 4351 | 12 24 01.6 | 12 12 18 | Sc(s) II.3 | SB(rs)ab: pec | 0.37 | T/N[s] | 10.44 | $-21.1 \pm 0.1$ | 92 | 47 | 65 | 2317 ± 16 | 1.7 | $20.3 \pm ^{0.8}_{1.2}$ |
| NGC 4424 | 12 27 11.5 | 09 25 15 | Sa pec | SB(s)a: | 0.42 | T/C | 9.17[a] | $-21.7 \pm 0.3$ | 125 | 60 | 88 | 440 ± 6 | 3.1 | $15.2 \pm 1.9$ |
| NGC 4429 | 12 27 26.4 | 11 06 29 | $S0_3(6)$/Sa pec | SA(r)0$^+$ | 0.54 | T/A | 6.76 | $-24.3 \pm 0.1$ | 220 | 60 | 89 | 1127 ± 31 | 1.5 | $16.3 \pm 0.9$ |
| NGC 4450 | 12 28 29.3 | 17 05 07 | Sab pec | SA(s)ab | 0.49 | T/A | 6.90 | $-23.6 \pm ^{0.1}_{0.2}$ | 205 | 46 | 179 | 1958 ± 6 | 4.7 | $12.6 \pm ^{1.0}_{0.6}$ |
| NGC 4457 | 12 28 59.3 | 03 34 16 | RSb(rs) II | (R)SAB(s)0/A | 0.66 | T/N[s] | 7.96 | $-23.1$ | 160[b] | 34 [c] | 79[d] | 881 ± 14 | 8.8 | 16[e] |
| NGC 4569 | 12 36 49.8 | 13 09 46 | Sab(s) I-II | SAB(rs)ab | 0.43 | T/N[s] | 6.77 | $-23.80 \pm 0.01$ | 266 | 64 | 26 | −232 ± 22 | 1.7 | $13.0 \pm 0.1$[f] |
| NGC 4580 | 12 37 48.6 | 05 22 06 | Sc/Sa | SAB(rs)a pec | 0.41 | T/N[s] | 8.77 | $-22.95 \pm 0.05$ | 87 | 45 | 154 | 1036 ± 7 | 7.2 | $22.1 \pm 0.5$ |
| NGC 4606 | 12 40 57.6 | 11 54 44 | Sa pec | SB(s)a: | 0.42 | T/C | 9.30 | $-22.20 \pm ^{0.05}_{0.11}$ | 103 | 67 | 44 | 1655 ± 16 | 2.5 | $19.9 \pm ^{1.0}_{0.5}$ |
| NGC 4651 | 12 43 42.6 | 16 23 36 | Sc(r) I-II | SA(rs)c | 0.55 | N | 8.25 | $-23.90 \pm ^{0.10}_{0.04}$ | 157 | 51 | 72 | 804 ± 10 | 5.1 | $26.9 \pm ^{0.5}_{1.2}$ |
| NGC 4694 | 12 48 15.1 | 10 59 00 | Amorph | SB0 pec | 0.62 | T/C | 9.03 | $-21.6 \pm 0.2$ | 120 | 42 | 146 | 1177 ± 11 | 4.5 | $13.4 \pm ^{1.3}_{1.0}$ |
| NGC 4698 | 12 48 23.0 | 08 29 14 | Sa | SA(s)ab | 0.51 | A | 7.43 | $-24.50 \pm ^{0.83}_{0.41}$ | 187 | 62 | 169 | 1005 ± 15 | 5.8 | $24.3 \pm ^{5.1}_{4.2}$[g] |

**Notes.** (1) Galaxy name; (2) right ascension in hours, minutes, and seconds; (3) declination in degrees, minutes, and seconds; (4) Hubble Types from Bingelli et al. (1987, hereafter BST), Sandage & Tammann (1987), or Sandage & Bedke (1994); (5) Hubble type from de Vaucouleurs et al. (1991, hereafter RC3); (6) central $R$ light concentration parameter (Koopmann et al. 2001); (7) star formation class from Koopmann & Kenney (2004); (8) apparent magnitude in $H$ band (Gavazzi et al. 1999); (9) absolute magnitude in $H$ band (Cortés et al. 2008); (10) radius in units of arcseconds at the 25 R mag arcsec$^{-2}$ isophote (Koopmann et al. 2001); (11) inclination from Koopmann et al. (2001); (12) optical PA at $R_{25}$ (J. R. Cortés et al., in preparation); (13) heliocentric radial velocity from HyperLEDA; (14) the projected angular distance in degrees of the galaxy from M87; (15) line-of-sight distance (Cortés et al. 2008).
[a] 2MASS Galaxy Atlas, Jarrett et al. (2003).
[b] Extrapolation from the $R$-band light profile.
[c] HyperLEDA database.
[d] Measured at $100'' \sim 0.6R_{25}$.
[e] Virgo Cluster distance.
[f] Stellar-kinematics-based distance considering dark matter halo from Cortés et al. (2008).
[g] H I-based distance from Solanes et al. (2002).

galaxies may be in the process of morphological transformation, and could be considered as "snapshots" in the evolutionary path from actively star-forming spiral galaxies to more passive spirals and lenticulars.

With these objectives in mind, in this work, we present a study of the stellar and ionized gas kinematics of 13 peculiar Virgo cluster galaxies using integral-field spectroscopy techniques. We profit from the ability of this technique to accurately map two-dimensional (2D) velocity fields for both the stars and the ionized gas in the centers of these galaxies. This data set has previously been used to estimate the three-dimensional (3D) cluster locations of all sample galaxies by using stellar kinematics to derive their distances (Cortés et al. 2008), and for a detailed investigation of the nature of two of the most peculiar galaxies of the present sample, NGC 4064 and NGC 4424 (e.g., Cortés et al. 2006).

The present paper is structured as follows. A brief description of the galaxy sample is given in Section 2. The observation and data reduction procedures are summarized in Section 3. A description of the observed stellar and ionized gas kinematics is presented in Section 4. In Section 5, we summarize the kinematical peculiarities observed in these galaxies. In Section 6, we discuss the velocity dispersion profiles and kinematical support of these galaxies. In Section 7, we compare our observations with simulations of merger remnants, ICM-ISM stripped galaxies, and tidal interactions. These results are discussed from the perspective of galaxy evolution in clusters in Section 8. We summarize our results and present our conclusions in Section 9. A discussion of individual galaxies is given in the Appendix.

## 2. THE GALAXY SAMPLE

The sample consists of 13 peculiar Virgo cluster spiral galaxies spanning a variety of optical morphologies (Figure 1, Table 1). Morphological selection was performed using the R and H$\alpha$ atlas of Virgo cluster galaxies of Koopmann et al. (2001), whereas the kinematical selection made use of the published H$\alpha$ kinematics of 89 Virgo cluster spirals by Rubin et al. (1999). While the sample selection is not uniform, it is designed to include bright Virgo spirals whose peculiarities are most poorly understood, and to include representatives of the different H$\alpha$ types identified by Koopmann & Kenney (2004). In choosing sample galaxies within a given H$\alpha$ type, we gave preference to those with kinematical peculiarities.

In Virgo spirals, there is a poor correlation between the bulge-to-disk ratio and the normalized star formation rate so that the Hubble classification of spirals does not work well in the Virgo Cluster (Koopmann & Kenney 1998). The Hubble-type classification assigned to Virgo galaxies generally reflects the star formation rate rather than the bulge-to-disk ratio, so that Virgo spirals with reduced star formation rates are generally classified as early-type spirals, independent of their bulge-to-disk ratio. Our sample includes more early-type than late-type galaxies, since most of the strongly disturbed cluster galaxies have reduced star formation rates and so are classified as early types. Since the Hubble classifications of cluster spirals do not capture the intrinsic variation in galaxy morphologies, either the distributions of old stellar light or the young stars, we use instead the light concentration parameter $C_{30}$ (Abraham et al.

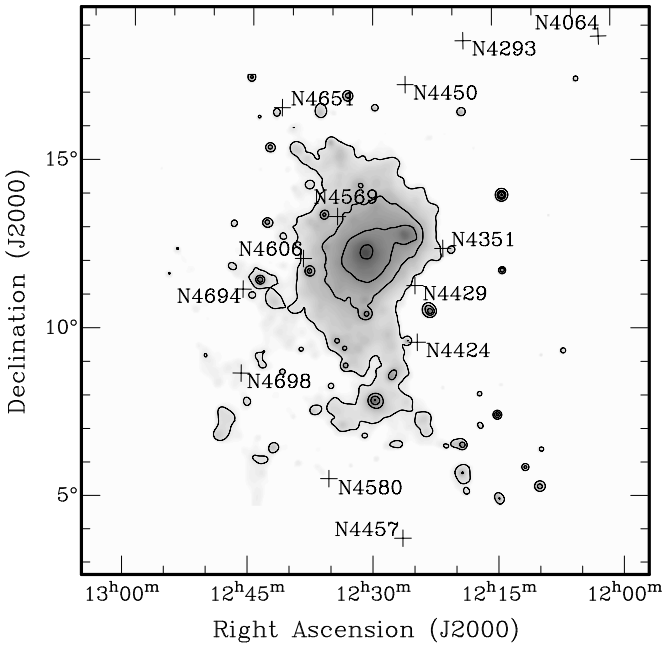


**Figure 1.** Sample galaxies and their location in the Virgo Cluster. The contour map represents the *ROSAT* X-ray emission in the cluster (Böhringer et al. 1994). Sample galaxies are represented by a black plus sign and its NGC name.

1994) as an objective measure of the bulge-to-disk ratio, and the Hα type (Koopmann & Kenney 2004) to describe the radial distribution of star formation.

Since Hα types seem to correlate with the type of interaction experienced by the galaxy (Koopmann & Kenney 2004), and also with some kinematical properties that we describe in this paper, here we provide brief definitions of these categories and indicate to which category our sample galaxies belong.

1. *Normal:* NGC 4651. In Normal galaxies, the Hα radial distribution is close to the mean of isolated spirals, both in the shape of the radial distribution (which is close to the R light profile) and in amplitude.
2. *Truncated/Normal:* NGC 4351, NGC 4457, NGC 4569, and NGC 4580. In Truncated/Normal galaxies, the Hα radial distribution is similar to that in a Normal galaxy out to a well-defined truncation radius, but there is virtually no Hα emission beyond.
3. *Truncated/Compact:* NGC 4064, NGC 4424, NGC 4606, and NGC 4694. In Truncated/Compact galaxies, the Hα radial profile is much steeper than the R light profile at all radii, with a strong central peak and a very sharp drop with radius, such that there is virtually no emission beyond the central 1 kpc. In Koopmann & Kenney (2004), this category also included the provision that the central Hα intensity was much higher than Normal, but here we relax this provision. Thus we include NGC 4694[7] in this category, which has an Hα radial profile like the other T/C galaxies but with a lower amplitude.
4. *Anemic or Truncated/Anemic galaxies:* NGC 4293, NGC 4429, NGC 4698, and NGC 4450. In Anemic galaxies, the shape of the Hα radial distribution is similar to that of a Normal galaxy (and like the R light profile), but with a much lower amplitude. Anemic galaxies have weak but detectable emission over much of the stellar disk. Truncated/Anemic galaxies have an anemic distribution out to a well-defined truncation radius, but virtually no Hα emission beyond. Whereas most of our sample galaxies in these categories have Hα emission detected out to at least $0.3R_{25}$, we also include in the Truncated/Anemic category the S0 galaxy NGC 4429, which has a very small and very weak Hα disk.

Distances to many individual early-type Virgo galaxies have now been measured to good accuracy, based on the surface brightness fluctuation method. The mean distance to early-type Virgo cluster galaxies is 16.5 ± 0.1 mpc (Mei et al. 2007). The distances to late-type and peculiar Virgo galaxies are less accurately known. The commonly used Tully–Fisher method based on H I line-widths works well for most late-type galaxies, but produces erroneous distances for a subset of cluster galaxies that are H I-poor and disturbed (Cortés et al. 2008). In Cortés et al. (2008), we derived distances to galaxies in the present Virgo sample based on a new approach using a stellar kinematics-based version of the Tully–Fisher relation. It is revealing to compare different distance estimates for perhaps the most disturbed galaxy in our sample, NGC 4424. The H I-based Tully–Fisher method provides a distance of 4.8 mpc (Solanes et al. 2002), our stellar-kinematics-based Tully–Fisher relation provides a distance of 15.2 mpc (Cortés et al. 2008), and a recent Type Ia supernova provides a distance of 15.5 mpc (Munari et al. 2013). While this is an extreme example, it illustrates that our stellar-kinematics-based Tully–Fisher distances may be relatively accurate. We adopt these distances in this paper and present them in Table 1.

## 3. OBSERVATIONS, DATA REDUCTION, AND METHODS

### *3.1. Observations and Data Reduction*

The galaxies were observed using the DensePak Integral-field unit (Barden et al. 1998) installed at the 3.5m WIYN telescope at Kitt Peak. The DensePak array consists of 90 fibers with a diameter of 3.″5, and about 4″ separation with a covering area of 30″×45″, which corresponds to 2.3 × 3.5 kpc at the mean Virgo distance. The observations were taken in three observing runs during 1999 April 8–9th, 2001 May 24–25th 2001, and 2002 February 10–12th. The 860 line mm$^{-1}$, blaze angle 30.°9 grating at 5000 Å was used to second order, covering the 4500–5500 Å wavelength range with a spectral dispersion of 0.48 Å per pixel and a spectral resolution of 2.02 Å. The DensePak array, in most cases, was oriented along the optical major axis of the galaxies (Table 2, Figure 2). Details about the exposure time used to observe the galaxies are given in Table 2. Radial velocity standards stars (Barbier–Brossat & Figon 2000) were observed as spectral templates with an exposure time of 180 s. Details about each star are presented in Table 3.

The spectra were reduced in the usual manner with IRAF reduction for multi–fiber spectrographs. They were zero-subtracted and overscan-corrected with the standard IRAF tasks. The flat fielding correction, sky subtraction, fiber throughput correction, and wavelength calibration were carried out using the IRAF task DOHYDRA in the package HYDRA.[8] Alignment between different exposures was checked by comparing the continuum maps between each exposure. The exposures were aligned using our own program written in IDL.[9] After

[7] In Koopmann & Kenney 2004, NGC 4694 was classified as T/N, but re-inspection of the Hα radial profile shows that it does not match the T/N criteria and is better described by the modified T/C definition proposed here.

[8] F. Valdez 1995, Guide to the HYDRA Reduction Task DOHYDRA, available at http://iraf.net/irafdocs/dohydra.pdf.

[9] www.exelisvis.com/ProductsServices/IDL.aspx

**Table 2**
DensePak Observation Logs

| Name | Dates | $PA_{DensePak}$ (°) | $T_{exp}$ (s) |
|---|---|---|---|
| (1) | (2) | (3) | (4) |
| NGC 4604 | 1999 Apr 8 | 150 | 4 × 1800 |
| NGC 4293 | 2002 Feb 11–12 | 72 | 1800, 2 × 1800 |
| NGC 4351 | 2001 May 25 | 80 | 4 × 1800 |
| NGC 4424 | 1999 Apr 9 | 90 | 6 × 1800 |
| NGC 4429 | 2002 Feb 12 | 99 | 2 × 1800 |
| NGC 4450 | 2002 Feb 12 | 175 | 4 × 1800 |
| NGC 4457 | 2002 Feb 11 | 0 | 4 × 1800 |
| NGC 4569 | 2001 May 24 | 0 | 4 × 1800 |
| NGC 4580 | 2002 Feb 11 | 158 | 4 × 1800 |
| NGC 4606 | 2002 Feb 12 | 33 | 4 × 1800 |
| NGC 4651 | 2001 May 24 | 71 | 4 × 1800 |
| NGC 4694 | 1999 Apr 9 | 140 | 3 × 1800 |
| NGC 4698 | 2002 Feb 10 | 170 | 4 × 1800 |

**Notes.** (1) Galaxy name; (2) observation date; (3) PA of the DensePak array (taken from Koopmann et al. 2001); (4) exposure time.

**Table 3**
Characteristics of Template Stars

| Name | Template Star | Spectral Type | ($km\ s^{-1}$) (4) $V_{helio}$ |
|---|---|---|---|
| (1) | (2) | (3) | |
| NGC 4064 | HD 90861 | K2 III | 37.13 |
| NGC 4293 | HD 69632 | K0 III | −0.90 |
| NGC 4351 | HD 159479 | K2 III | −24.6 |
| NGC 4424 | HD 86801 | G0 V | −14.5 |
| NGC 4429 | HD 69632 | K0 III | −0.90 |
| NGC 4450 | HD 69632 | K0 III | −0.90 |
| NGC 4457 | HD 35005 | G7 III | 25.90 |
| NGC 4569 | HD 159479 | K2 III | −24.6 |
| NGC 4580 | HD 35005 | G7 III | 25.90 |
| NGC 4606 | HD 35005 | G7 III | 25.90 |
| NGC 4651 | HD 159479 | K2 III | −24.6 |
| NGC 4694 | HD 90861 | K2 III | 37.13 |
| NGC 4698 | HD 77823 | K2 III | 65.90 |

**Notes.** (1) Galaxy name; (2) template star name; (3) template star spectral type; (4) heliocentric radial velocity (Barbier–Brossat & Figon 2000).

the alignment, the galaxy spectra were averaged to improve the signal-to-noise ratio and remove cosmic rays.

In two sample galaxies, NGC 4424 and NGC 4351, the spectra in many positions have a signal-to-noise ratio per pixel lower than the limit for obtaining reliable kinematics until the second moment (S/N ∼ 15). Therefore, spectra in these galaxies were binned using the adaptive scheme developed by Cappellari & Copin (2003), for achieving a signal-to-noise ratio good enough for obtaining reliable kinematics.

### 3.2. Stellar and Gas Kinematics

Stellar kinematics of the sample galaxies were derived by using the penalized pixel-fitting (pPXF) method developed by Cappellari & Emsellem (2004). This method allows the masking of emission lines, a more realistic estimation of errors than in other methods, and automation, allowing us to derive the kinematics of many spectra in a relatively short amount of time. Although the method can measure the Gauss-Hermite moments of the line-of-sight velocity distribution (LOSVD) up to $h_6$, the low signal-to-noise ratio of the spectra (S/N < 60) in most of our sample galaxies only allow us to obtain reliable measurements until the velocity dispersion ($\sigma$). We obtained Gauss-Hermite moments up to $h_4$ in only three sample galaxies: NGC 4429, NGC 4450, and NGC 4561. Template spectra were chosen from the spectra of observed radial velocity standard stars (typically G and K giants) that better fit the galaxy spectra. The pPXF method determines the broadening function (LOSVD) between the template star spectra and the galaxy spectra. If the instrumental dispersions between the template and the galaxy are different, then we need to convolve the template spectra by the square root of the quadratic difference between the instrumental dispersion of the galaxy and the template star. Since we observed the template stars and sample galaxies using the same observational setup during the same observing runs, and therefore the instrumental dispersions are the same for both, it was not necessary to convolve the template star and the derived velocity dispersion is already corrected by instrumental dispersion. A linear combination of different template star did not show any significant improvement in the fits. The heliocentric correction was applied to the derived line-of-sight velocities in each galaxy. Errors were estimated using a Monte-Carlo scheme. They were obtained as the standard deviation of the kinematical parameters ($V$ and $\sigma$) from many realizations ($N = 100$) of the input spectra by adding Gaussian noise to a model galaxy spectrum. Comparison between the galaxy spectra in the central region and the model galaxy spectra obtained by pPXF from the template star spectra are shown in Figure 3.

2D ionized gas kinematics were derived from the emission lines (H$\beta$ and [O III] $\lambda$5007) by fitting a Gaussian function to the emission lines in the continuum subtracted spectra, thereby obtaining $V$ and $\sigma$ for the ionized gas. Finally, we applied a heliocentric correction to the derived gas velocities. In this work, we focus only on the ionized gas line-of-sight velocity.

### 3.3. Kinematic Parameter Determination

Systemic velocities, kinematic position angles, and rotational velocities were obtained for each galaxy by fitting a pure circular tilted ring model (Begeman 1989) to the stellar and ionized gas velocity fields in cases where this was possible.

The method consists of dividing the galaxy into a set of concentric rings, each ring being characterized by a fixed value of the inclination $i$, the rotation velocity $V_{rot}$, and the kinematic position angle $\phi$. We define the sky coordinates $(x, y)$ as the DensePak array coordinates with $x$ oriented over the position angle of the DensePak array $\phi_{DensePak}$ (see Table 2). For a given ring, the observed radial velocities recorded on a set of sky-coordinates are given by

$$V_{obs}(x, y) = V_{sys} + V_{rot}(R)\sin(i)\cos(\theta), \quad (1)$$

where $\theta$ is the azimuthal angle in the plane of the galaxy, measured from the optical major axis of the galaxy. It can be shown that for any point $(x_{gal}, y_{gal})$ in the plane of the galaxy, $\theta$ is given by

$$\cos(\theta) = \frac{x_{gal}}{R} = \frac{(x - x_0)\cos(\phi - \phi_{DensePak}) + (y - y_0)\sin(\phi - \phi_{DensePak})}{R}, \quad (2)$$

$$\sin(\theta) = \frac{y_{gal}}{R} = \frac{(y - y_0)\cos(\phi - \phi_{DensePak}) - (x - x_0)\sin(\phi - \phi_{DensePak})}{R\cos(i)}, \quad (3)$$

where $R$ is the mean radius of the ring in the plane of the galaxy and $(x_0, y_0)$ are the sky coordinates of the center of the ring.

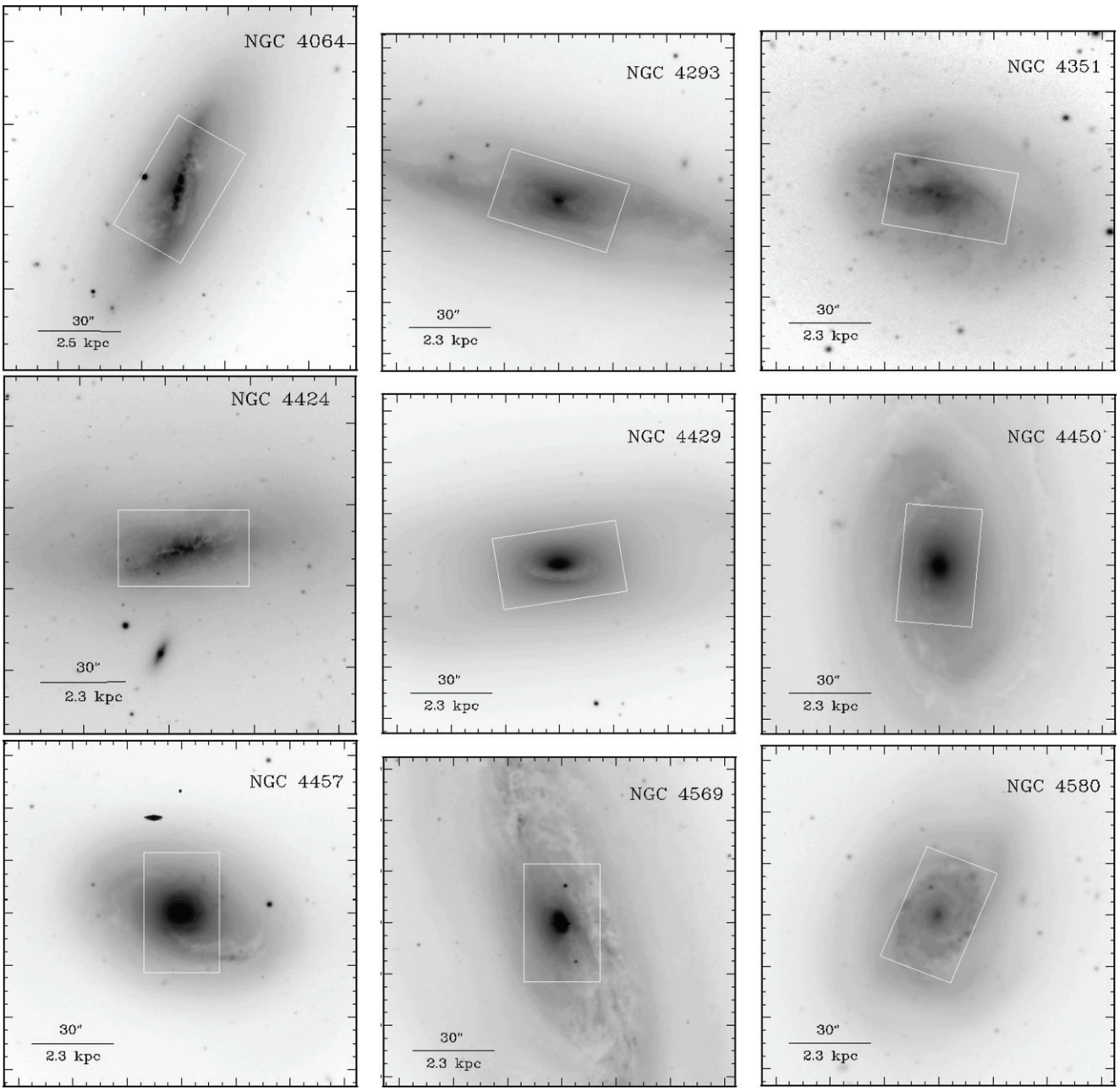


**Figure 2.** *R*-band WIYN mini-mosaic images for some sample galaxies and the DensePak array. Image sizes are about $2' \times 2'$, with the usual orientation of north up and east to the left. The white rectangle represents the DensePak array as it was oriented in the sky.

In this work, we define the position angle (either optical or kinematic) as the angle between the optical/kinematic major axis of the galaxy and the line from the galaxy center headed North, measured from north to east.

The procedure is iterative, and described as follows. (1) We divide the galaxy into concentric rings with typical widths of one fiber on the major axis. (2) For each ring, we make a least-square fit of $V_{\rm obs}$ with $x_0$, $y_0$ and $V_{\rm sys}$ as free parameters, keeping $V_{\rm rot}$, $\phi$, and $i$ fixed. Then, we took as center coordinates and systemic velocity the mean values over all of the rings. (3) After this, we kept $x_0$, $y_0$ and $V_{\rm sys}$ fixed, and we fitted the values $V_{\rm rot}$ and $\phi$ simultaneously. We did not attempt to fit the inclination $i$ as it was difficult to disentangle the degeneracy between $i$ and $V_{\rm rot}$, so we kept this parameter fixed to its optical value as derived from Koopmann et al. (2001) for all the rings. (4) The improved values define a new systemic velocity $V_{\rm sys}$ and set of sky coordinates $x_0$, $y_0$. Repeat (2) and (3) with these parameters until convergence is obtained.

On average, we have six degrees of freedom in each annuli. We are aware that points close to the minor axis carry less information about the rotational velocity, so we used a weighting function of $|\cos(\theta)|$ in order to give more weight to points close to the major axis.

Stellar rotation curves were obtained for all of the galaxies in the sample. Kinematic parameters derived from the stellar velocities are presented in Table 4. Stellar rotation curves are not corrected for asymmetric drift, since this is beyond of the scope of this paper. This correction requires solution of the collisionless Boltzmann equation. Stellar circular velocities for these galaxies are presented in Cortés et al. (2008). The case of NGC 4064 was complicated since this galaxy has a strong central bar, and a model based on a pure circular disk is not fully

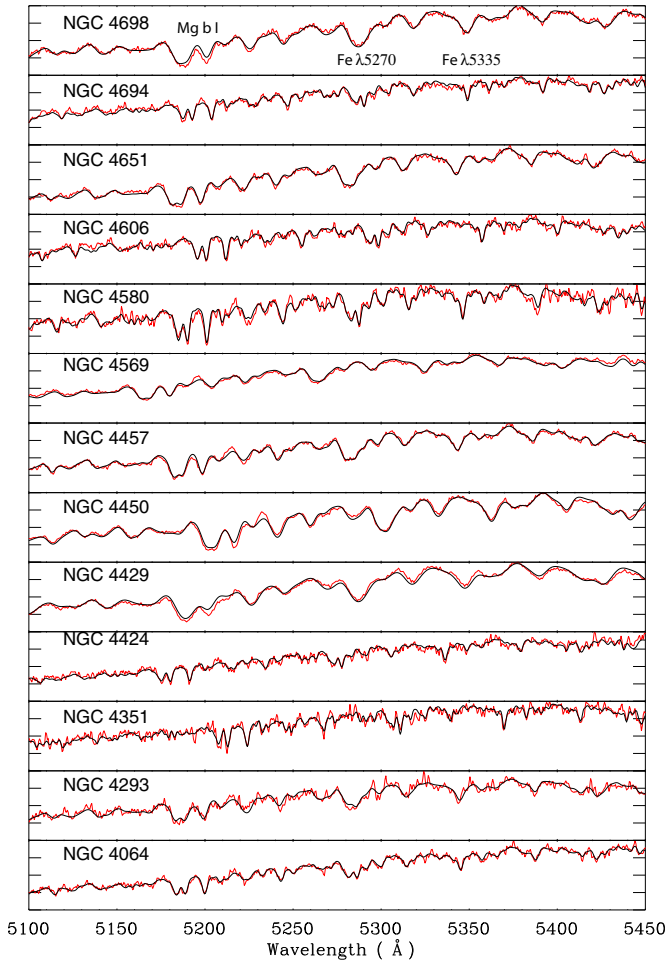


**Figure 3.** Spectra of the center of the sample galaxies and best pPXF model spectra. Galaxy spectra are represented by thick red lines, pPXF model spectra are represented by solid black lines. Mg b I lines and Fe lines are clearly visible.

justified but this approach is useful for separating the circular streaming component from the radial streaming component.

We obtained ionized gas rotation curves for six galaxies in the sample. We were unable to fit a pure circular tilted ring model to the ionized gas velocity fields for some galaxies due to scarcity of emission (e.g., NGC 4424, NGC 4606, or NGC 4694) or large non-circular motions (e.g., NGC 4064, NGC 4569, and NGC 4457). However, systemic ionized gas velocities were estimated for all of the galaxies, either by taking the mean of the averaged LOS velocities at the same radius on opposite sides along the major axis, or by considering the LOS velocity at the position of the peak of the stellar continuum map. The kinematic parameters derived from ionized gas velocities are presented in Table 5.

In some of our galaxies, the optical and/or kinematic position angles vary with radius, or there are misalignments between the optical and/or kinematic position angles. We discuss these variations in Section 5.1.

### *3.4. Comparison with the Literature*

Eight galaxies in our sample have published stellar kinematic data from other groups. In general, the results are consistent given the difference in spatial resolution between our DensePak data (3.″5) and that for the other groups (0.″6–1.″2).

Four galaxies have published long-slit stellar kinematics: NGC 4429 (Simien & Prugniel 1997), NGC 4450, NGC 4569 (Fillmore et al. 1986), and NGC 4698 (Héraudeau et al. 1999, Bertola et al. 1999). A comparison of our data with the data from these groups for the LOS velocity and velocity dispersion along the major axis is shown in Figure 4. In NGC 4429, our stellar velocity data show a good correspondence with the Simien & Prugniel data, although our velocity dispersions are slightly higher due to our lower spatial resolution. In NGC 4450, there are some disagreements between our data and the Fillmore et al. data which do not seem attributable to differences in spatial resolution. Since they did not publish any information about their errors, we do not know if the differences are significant. In the case of NGC 4569, the Fillmore et al. data exhibit a peak in the stellar velocity at 3″ that we do not resolve due to our lower spatial resolution. Both data sets seems consistent in their velocity dispersion measurements. In NGC 4698, our data seem consistent with the Héraudeau et al. data within the errors.

Long-slit minor axis stellar kinematics published by Coccato et al. (2005) for NGC 4064 and NGC 4424 seem consistent with our stellar kinematic measurements. 2D stellar kinematics for NGC 4293 and NGC 4698 were obtained by the SAURON project (Falcón–Barroso et al. 2006). Our stellar velocity and velocity dispersion fields are similar to theirs, with differences inherent to the different spatial resolutions between SAURON and DensePak (0.″94 for SAURON and 3.″5 for DensePak). Mazzalay et al. (2014) presented a 3″×3″ Br$\gamma$ stellar velocity field with SINFONI, with a high spatial resolution (∼0.″25). This map exhibits a higher amplitude in velocity within the inner 3″ and a lower velocity dispersion, which is expected due to the huge difference in the spatial resolutions between the two maps.

Long-slit ionized gas kinematics (H$\alpha$) have been published by Rubin et al. (1999). In Figure 5, we present a comparison between Rubin's H$\alpha$ long-slit kinematics and our ionized gas LOS velocities (H$\beta$, and [O III] λ5007) along the major axis for nine sample galaxies. Our ionized gas velocities show good correspondence with Rubin's data, although in NGC 4651 our ionized gas velocities display an apparent lower rotation velocity. This could be due to the different spatial resolution between the long-slit spatial scale (2″) and DensePak (3.″5), which will smear out DensePak velocities. There are also some systematic differences between [O III] velocities and H$\alpha$ velocities for NGC 4694 and NGC 4698. We do not know the cause of these differences. 2D ionized gas velocity fields have been obtained by Chemin et al. (2006) in H$\alpha$ for NGC 4351, NGC 4450, NGC 4569, and NGC 4580. H$\beta$ velocity fields look similar to the H$\alpha$ velocity fields, but with differences inherent to the different spatial resolution (∼1″ for Chemin et al.) and signal-to-noise ratio since H$\alpha$ is much more intense than H$\beta$ emission. Falcón–Barroso et al. (2006) also presented H$\beta$ and [O III] ionized gas velocity fields for NGC 4293 and NGC 4698. We were not able to detect any gas emission in NGC 4293. In NGC 4698, both [O III] velocity fields seem consistent, with differences inherent to the different spatial resolutions between SAURON and DensePak.

The works of Chemin et al. (2006) and Falcón–Barroso et al. (2006) have determined kinematic PAs for some of our sample galaxies. Chemin et al. (2006) presented H$\alpha$ kinematic PAs for NGC 4351, NGC 4450, NGC 4457, NGC 4569, and NGC 4580. For NGC 4351, we derived (see Section 5.1) $PA_{kin}$ H$\beta = 62° \pm 16°$, which is consistent with $PA_{kin}$ H$\alpha = 73° \pm 5°$ from Chemin et al. (2006). Both gas kinematic PAs are different

**Table 4**
Parameters and Derived Quantities for the Stellar Velocity Fields

| Name | $V_{sys}$ (km s$^{-1}$) | $PA_{outer}$ (°) | $PA_{inter}$ (°) | $PA_{kin}$ (°) | $\Psi_{outer}$ (°) | $\Psi_{inter}$ (°) | $V_{rot}$ (km s$^{-1}$) | $R_{max}$ (arcsec) |
|---|---|---|---|---|---|---|---|---|
| (1) | (2) | (3) | (4) | (5) | (6) | (7) | (8) | (9) |
| NGC 4064 | 929 ± 3 | 148 | 152 | 129[a] ± 15 | 19 ± 15 | 23 ± 15 | 72 ± 7 | 25 |
| NGC 4293 | 926 ± 4 | 62 | 72 | 42 ± 8 | 20 ± 8 | 30 ± 8 | 105 ± 10 | 27 |
| NGC 4351 | 2310 ± 2 | 65 | 70 | 53 ± 8 | 12 ± 8 | 17 ± 8 | 41 ± 19 | 20 |
| NGC 4424 | 442 ± 4 | 88 | 96 | 87 ± 8 | 1 ± 8 | 9 ± 8 | 31 ± 4 | 25 |
| NGC 4429 | 1094 ± 6 | 89 | 97 | 87 ± 3 | 2 ± 3 | 10 ± 3 | 136 ± 9 | 25 |
| NGC 4450 | 1953 ± 2 | 178 | 173 | 166[b] ± 5 | 12 ± 5 | 7 ± 5 | 114 ± 6 | 25 |
| NGC 4457 | 881 ± 2 | ... | 77 | 70 ± 3 | ... | 7 ± 3 | 83 ± 5 | 20 |
| NGC 4569 | −222 ± 6 | 26 | 19 | 32 ± 6[c] | 6 ± 6 | 13 ± 6 | 103 ± 3 | 25 |
| NGC 4580 | 1031 ± 4 | 154 | 160 | 158 ± 4 | 4 ± 4 | 2 ± 4 | 103 ± 8 | 25 |
| NGC 4606 | 1636 ± 5 | 44 | 39 | 39 ± 4 | 5 ± 4 | 0 ± 4 | 55 ± 4 | 25 |
| NGC 4651 | 784 ± 2 | 72 | 79 | 82 ± 4 | 10 ± 4 | 3 ± 4 | 178 ± 8 | 28 |
| NGC 4694 | 1174 ± 22 | 146 | 142 | 146 ± 6 | 0 ± 6 | 4 ± 6 | 63 ± 2 | 26 |
| NGC 4698 | 1025 ± 6 | 169 | 167 | 168[d] ± 3 | 1 ± 3 | 1 ± 3 | 116 ± 10 | 25 |

**Notes.** (1) Galaxy name; (2) heliocentric systemic velocity; (3) photometric PA at outer radii ($R_{25}$); (4) photometric PA at intermediate radii (0.5 $R_{25}$); (5) mean kinematical PA; (6) kinematical misalignment with respect to $PA_{outer}$; (7) kinematical misalignment with respect to $PA_{inter}$; (8) stellar rotation velocity at $R_{max}$; (9) most external point with reliable stellar rotation velocities.
[a] Strong non-circular motions due to central bar.
[b] The stellar kinematic PA in NGC 4450 changes from ∼175° in the central ∼10″ to ∼160° at $r$ ∼ 15–25″. This may reflect a change from the inner bulge-dominated region to the bar-dominated region at larger radius. There is good agreement between the stellar kinematic PA for $r$ <10″ and the photometric PA of the outer galaxy.
[c] The stellar velocity field of NGC 4569 is irregular. The SE side of the velocity map suggests a different PA than the NW side, perhaps due to dust extinction. The SE side suggests a kinematic PA closer to the photometric PA of the outer galaxy.
[d] The mean stellar kinematic PA given here is dominated by values for $r$ >10″, and so is not significantly influenced by the small orthogonally rotating bulge.

**Table 5**
Parameters and Derived Quantities for the Ionized Gas Velocity Fields

| Name | $V_{sys}$ Hβ (km s$^{-1}$) | $V_{sys}$ [O III] (km s$^{-1}$) | $PA_{kin}$ Hβ (°) | Ψ Hβ (°) | $PA_{kin}$ [O III] (°) | Ψ [O III] (°) | $V_{rot}$ Hβ (km s$^{-1}$) | $R_{max}$ Hβ (arcsec) | $V_{rot}$ [O III] (km s$^{-1}$) | $R_{max}$ [O III] (arcsec) |
|---|---|---|---|---|---|---|---|---|---|---|
| (1) | (2) | (3) | (4) | (5) | (6) | (7) | (8) | (9) | (10) | (11) |
| NGC 4064 | 943 ± 4 | 947[a] ± 2 | 150 | ... | ... | ... | 31 ± 9 | 12 | ... | ... |
| NGC 4351 | 2305 ± 3 | 2309 ± 2 | 62 ± 16 | 8 ± 16 | 62 ± 16 | 8 ± 16 | 66 ± 16 | 26 | 84 ± 6 | 28 |
| NGC 4450 | ... | 1960 ± 9 | ... | ... | 194 ± 8 | 19 ± 8 | ... | ... | 141 ± 23 | 20 |
| NGC 4457 | 858 ± 6 | 854 ± 6 | ... | ... | ... | ... | ... | ... | ... | ... |
| NGC 4569 | −294[a] ± 3 | −240 ± 4 | ... | ... | ... | ... | ... | ... | ... | ... |
| NGC 4580 | 1029 ± 3 | ... | 158 ± 4 | 0 ± 4 | ... | ... | 113 ± 10 | 24 | ... | ... |
| NGC 4606 | 1647[a] ± 1 | 1650[a] ± 3 | ... | ... | ... | ... | ... | ... | ... | ... |
| NGC 4651 | 778 ± 6 | 778 ± 4 | 79 ± 2 | 8 ± 2 | 76 ± 2 | 5 ± 2 | 213 ± 5 | 28 | 217 ± 10 | 28 |
| NGC 4694 | 1152 ± 2 | 1161 ± 3 | ... | ... | ... | ... | ... | ... | ... | ... |
| NGC 4698 | ... | 978[a] ± 7 | ... | ... | ... | ... | ... | ... | 163 ± 12 | 26 |

**Notes.** (1) Galaxy name; (2) Hβ systemic velocity; (3) [O III] systemic velocity; (4) Hβ kinematic PA; (5) Hβ kinematic PA misalignment; (6) [O III] kinematic PA; (7) [O III] kinematic PA misalignment; (8) Hβ rotation velocity at last measurement; (9) most external point with reliable Hβ rotation velocities; (10) [O III] rotation velocity at last measurement; (11) most external point with reliable [O III] rotation velocities.
[a] Velocity at central position of the array.

from the stellar kinematic $PA_{kin}$ = 53° ± 8°. NGC 4351 is a lopsided galaxy that may be experiencing ram pressure stripping, which may account for the difference in kinematic PAs between stars and gas. For NGC 4450, Chemin et al. give a gas (Hα) kinematic PA = 171° ± 7° in agreement with our stellar kinematic PA. For NGC 4457 and NGC 4580, Chemin et al.'s kinematic PAs are in agreement with our stellar kinematic PA. In the case of NGC 4569, our stellar kinematic PA is 32° ± 6°, which contrasts with 23° ± 4° derived by Chemin et al. Our stellar velocity field of NGC 4569 is irregular. The SE side of the velocity field suggests a different PA than the NW side, perhaps due to dust extinction. The SE side suggests a kinematic PA closer to the photometric PA of the outer galaxy, and therefore closer to the Chemin et al. PA determination. The stellar kinematic PA derived in the near-infrared for NGC 4569 (Mazzalay et al. 2014) is about 25°. This seems to confirm that our derivation of the stellar kinematic PA is affected by dust extinction. Falcón–Barroso et al. (2006) provide the differences between the photometric and kinematic PAs for NGC 4293 and NGC 4698. Their values are 30° for NGC 4293 and 3° for NGC 4698, which are in agreement with our determination of $\Psi_{inter}$ for both galaxies (see Table 4).

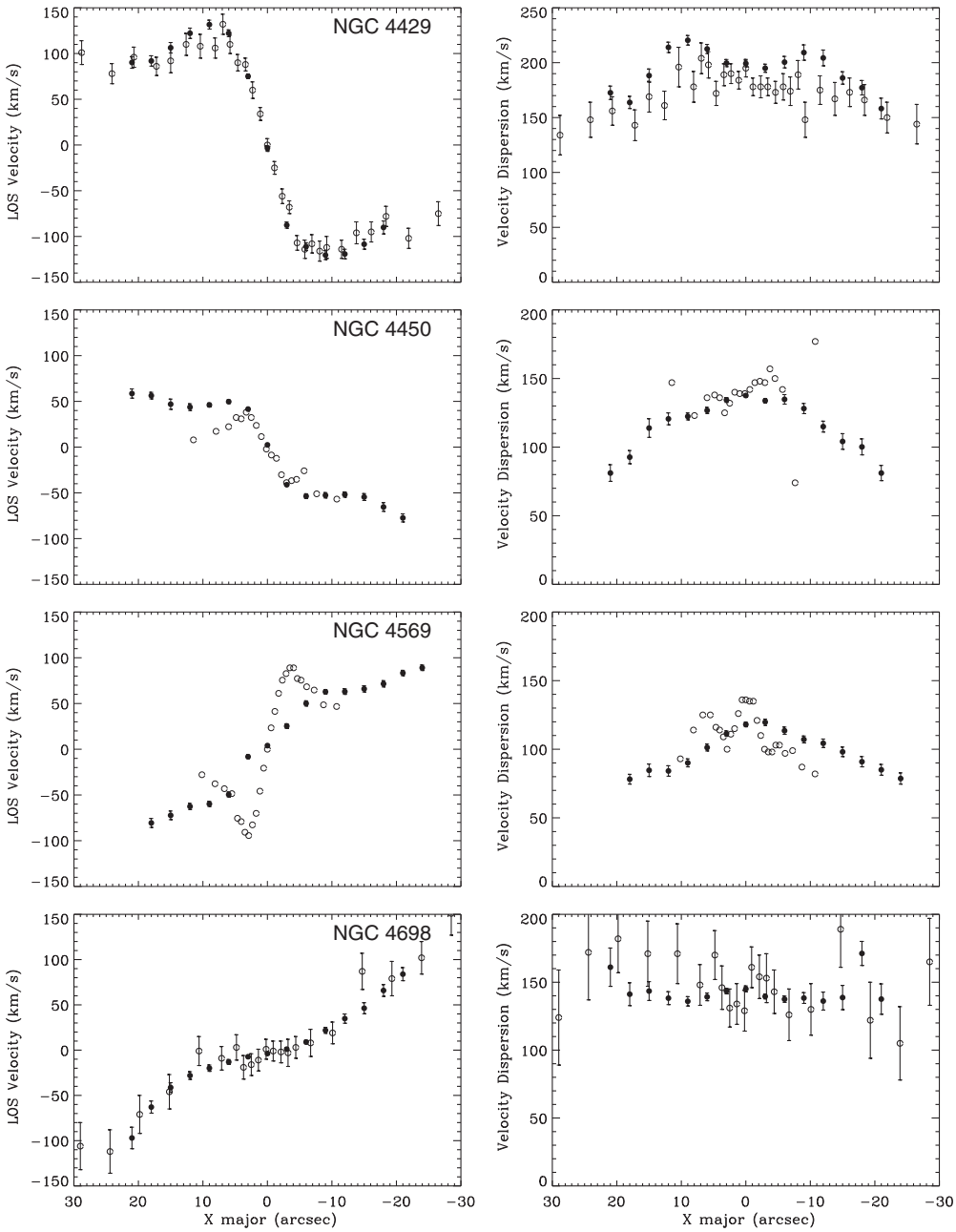


**Figure 4.** Comparison between the stellar kinematics of five sample galaxies with the values taken from the literature. Solid symbols represent our velocity determination, whereas open circles represent velocity determinations taken from the literature. From top to bottom: LOS mean velocities and velocity dispersion for NGC 4429, NGC 4450, NGC 4569, and NGC 4698. NGC 4429 published data were taken from Simien & Prugniel (1997), NGC 4450 and NGC 4569 published data were taken from Fillmore et al. (1986), and NGC 4698 from Héraudeau et al. (1999).

## 4. OBSERVED STELLAR AND GAS KINEMATICS

Figure 6 displays maps of the absorption and emission-line kinematics, as well as stellar continuum and emission line intensities for the 13 galaxies in our sample. The maps are displayed in order of increasing NGC number with the same scale and spatial resolution, and they are oriented with north up and east to the left. For each galaxy, we display (first row) the *R*-band image from the WIYN Telescope, maps of the distribution and kinematics of the H$\beta$ and [O III] $\lambda$5007 emission lines for all the galaxies where emission was detected (12/13), and ionized gas residual velocity maps where possible. The second row displays the continuum map (reconstructed by integrating the spectra within 5250 to 5450 Å), the mean stellar velocity field $V$, the stellar residual velocity map, the velocity dispersion field $\sigma$, and where possible the $h_3$ and $h_4$ moment maps. The open circles in both stellar and ionized gas maps represent broken fibers. The values at these positions were obtained by bilinear interpolation, but were used only for the purpose of display and were not used in the subsequent analysis. The crosses in the maps represent the positions of the peak in the continuum emission, and the straight line represents the optical PA of the galaxy obtained either by us or Koopmann et al. (2001). Also, in Figure 7, we present the stellar and ionized gas kinematics along the kinematic major and minor axes.

Detailed descriptions of the different galaxies are collected in the Appendix. Here, we concentrate on an overview of the general trends of the maps and the resulting velocity profiles.

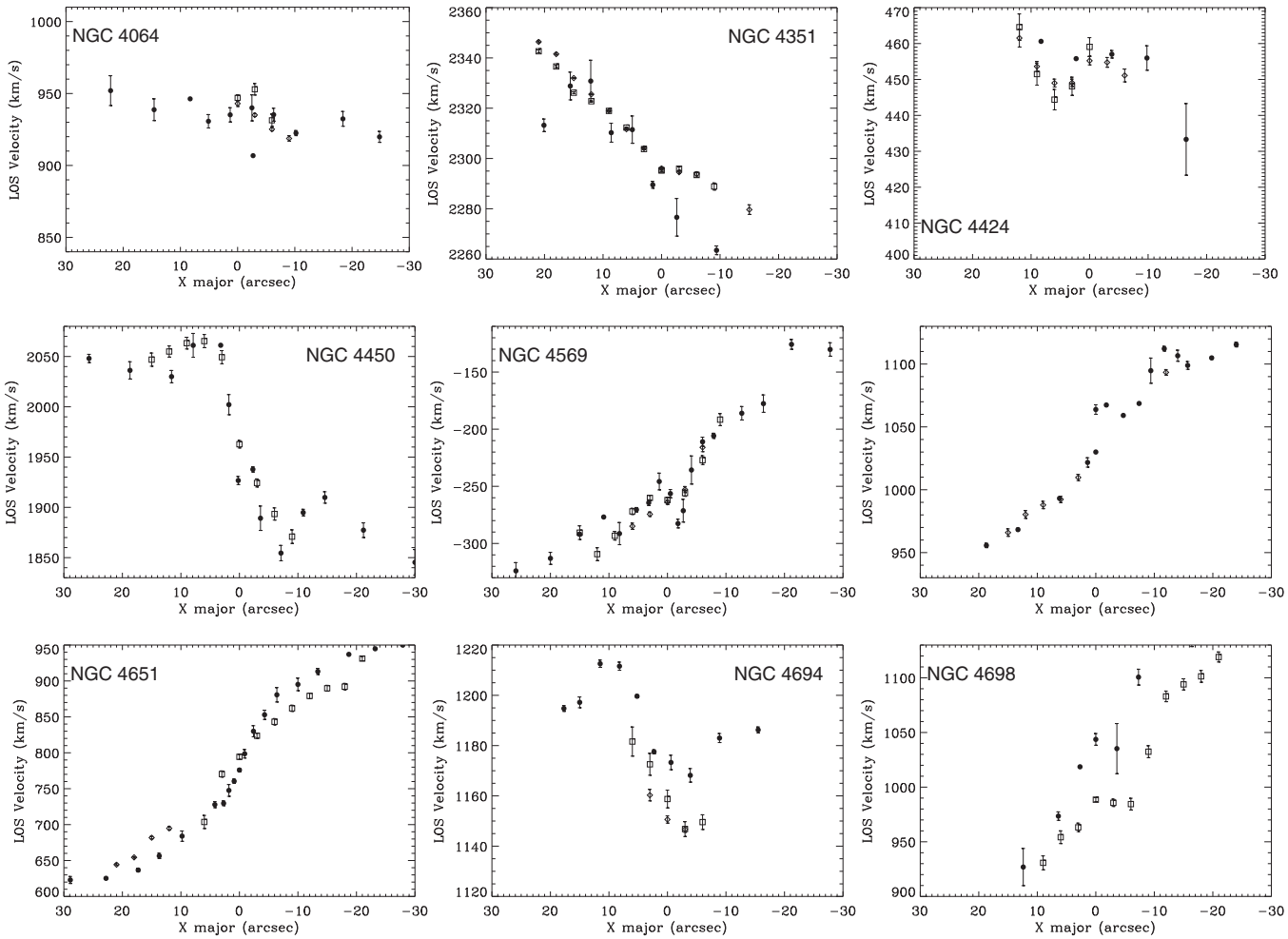


**Figure 5.** Comparison between the ionized gas kinematics along the major axis for nine sample galaxies with the values taken from the literature (Rubin et al. 1999). Solid symbols represent Rubin's H$\alpha$ velocities, whereas open diamonds represent our H$\beta$ velocity determination and open circles our [O III] velocity determinations.

### *4.1. Stellar and Ionized Gas Velocity Fields*

Stellar velocity fields in the galaxy sample exhibit a variety of interesting patterns. Regular stellar velocity fields consistent with pure circular motion are found in four galaxies: NGC 4429, NGC 4450, NGC 4580, and NGC 4651. Other galaxies display misalignments between the photometric and kinematic major axes, which suggest the presence of non-axisymmetric structures. Of these galaxies, NGC 4064 has S-shape isovelocity contours and other clear evidence of a strong stellar bar (Cortés et al. 2006), and we suspect that NGC 4293 also has a bar. Pinching of the central isovelocity contours, which is suggestive of cold circumnuclear stellar disks, is found in NGC 4429 and maybe in NGC 4450. Finally a remarkable twisting in the isovelocity contours is found in NGC 4698, which corresponds to a second kinematical component identified previously as an orthogonally rotating core by Bertola et al. (1999).

There is also variety in the patterns of stellar velocity dispersion. NGC 4450, NGC 4569, and NGC 4651 exhibit nearly symmetric velocity dispersion fields with a clear central peak, whereas NGC 4606, NGC 4694, and possibly NGC 4698 do not exhibit a clear central peak within the mapped region. Other galaxies (NGC 4064, NGC 4293, NGC 4424, and NGC 4429) display more asymmetric $\sigma$ patterns. NGC 4424 and NGC 4606, which have small bulges and are gravitationally disturbed, have off-nuclear, off-axis velocity dispersion peaks. Central drops in velocity dispersion, suggestive of cold circumnuclear stellar disks, are present in NGC 4429 and NGC 4694. The evidence for such a disk is particularly strong in NGC 4429, which shows pinched isovelocity contours in the same region.

The ionized gas velocity fields also exhibit a variety of patterns, and in general look more disturbed than the stellar velocity fields. Non-circular motions are found in NGC 4064, NGC 4351, NGC 4457, and NGC 4569. In NGC 4569, the ionized gas velocity field resembles the H$\alpha$ velocity field for NGC 2992 presented by Veilleux et al (2001), which shows a clear disk component plus blueshifted and redshifted components near the minor axis of the galaxy, interpreted as an outflow. We see similar features in our H$\beta$ and [O III] kinematic maps of NGC 4569, and we suggest that this is due to rotation plus an outflow component, although our detected ionized gas emission is sparse. Note that the high-resolution $H_2$ velocity field (FOV $\sim 2'' \times 2''$) presented by Mazzalay et al. (2014) also shows a blueshifted region toward the east side of the galaxy and it is interpreted as an outflow, which is consistent with the apparent blueshift in velocity found in the central position for the ionized gas (Table 5) with respect to the stars. An apparent difference of about 25° between the ionized gas and stellar kinematical PA is found in NGC 4450, even though both patterns are largely consistent with rotation. Evidence of a twisted gas disk is found in the center of NGC 4698, in the region of the orthogonally rotating bulge and the transition zone between the

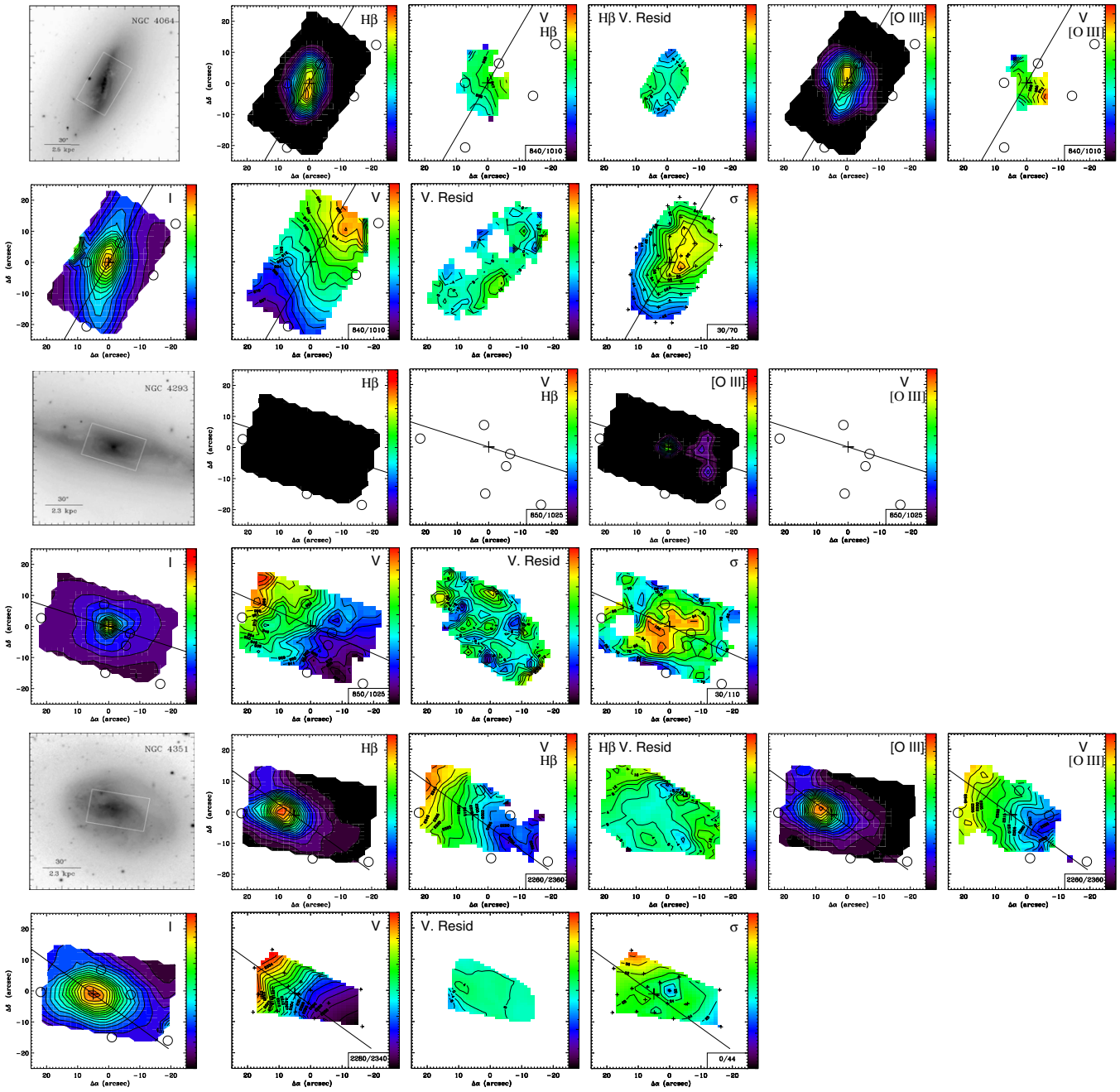


**Figure 6.** Maps of the stellar and ionized gas kinematics of the sample galaxies. Solid lines represent the optical PA of the galaxies. Crosses represent the position of the peak in the continuum map and open circles the dead fibers. The white rectangular box represents the area covered by DensePak. In the maps, north is up and east to the left. For each galaxy, we display the following. First row: the *R*-band image and where available H$\beta$ intensity map, H$\beta$ velocity field, H$\beta$ velocity residuals, [O III] $\lambda$ 5007 Å intensity map, [O III] $\lambda$ 5007 Å velocity field, and [O III] $\lambda$ 5007 Å velocity residuals. Second row: stellar reconstructed continuum map, stellar velocity field, stellar velocity residuals, stellar dispersion field, and where available $h_3$ and $h_4$ moment maps.

bulge-dominated and disk-dominated regions. The kinematic major axis of the gas varies as a function of radius and is very different from the kinematic major axis of the stars.

### *4.2. Stellar and Ionized Gas Rotation Curves, Stellar Velocity Dispersion, and $V/\sigma$ Radial Profiles*

Stellar and ionized gas rotation curves, as well as radial profiles of stellar velocity dispersion and $V/\sigma$ are shown in Figure 8. Residual maps between the observations and pure circular models are displayed in Figure 6. The velocity dispersion profiles were calculated by folding the stellar velocity dispersion along the kinematic major axis (given by $PA_{kin}$ in Table 4). Errors were estimated as the difference between the measured values and the mean of the velocity dispersions on the two sides of the galaxy. Velocity dispersion profiles are not corrected for inclination effects, as this requires a detailed model of the velocity ellipsoid which is beyond the scope of this work. The $V/\sigma$ radial profile was calculated as the ratio between the stellar rotation curve (corrected by inclination) and the velocity dispersion profile at the same galactocentric radius.

Rotation curves, stellar velocity dispersion, and $V/\sigma$ profiles for all of the sample galaxies are overplotted in Figure 9.

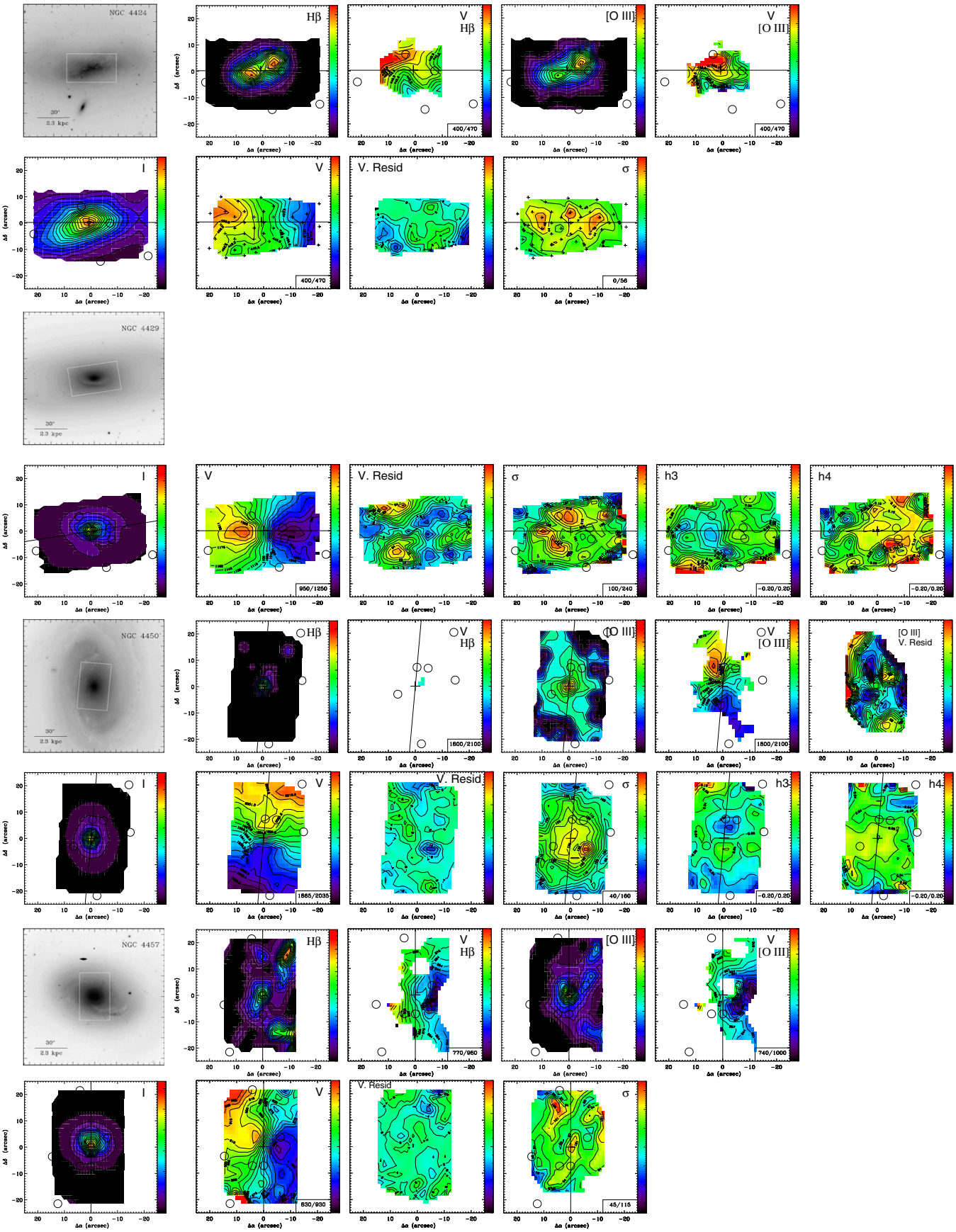


**Figure 6.** (Continued)

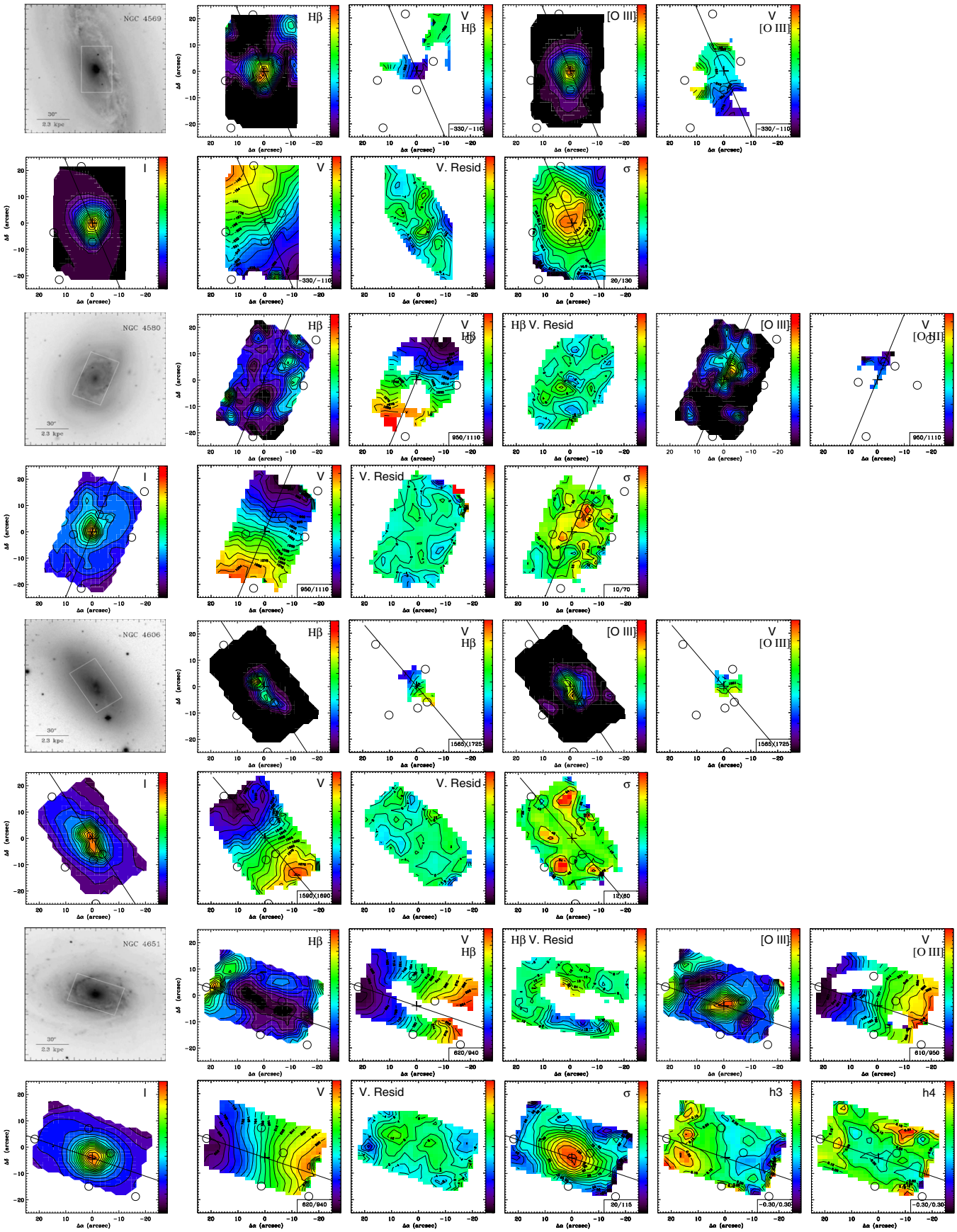


**Figure 6.** (Continued)

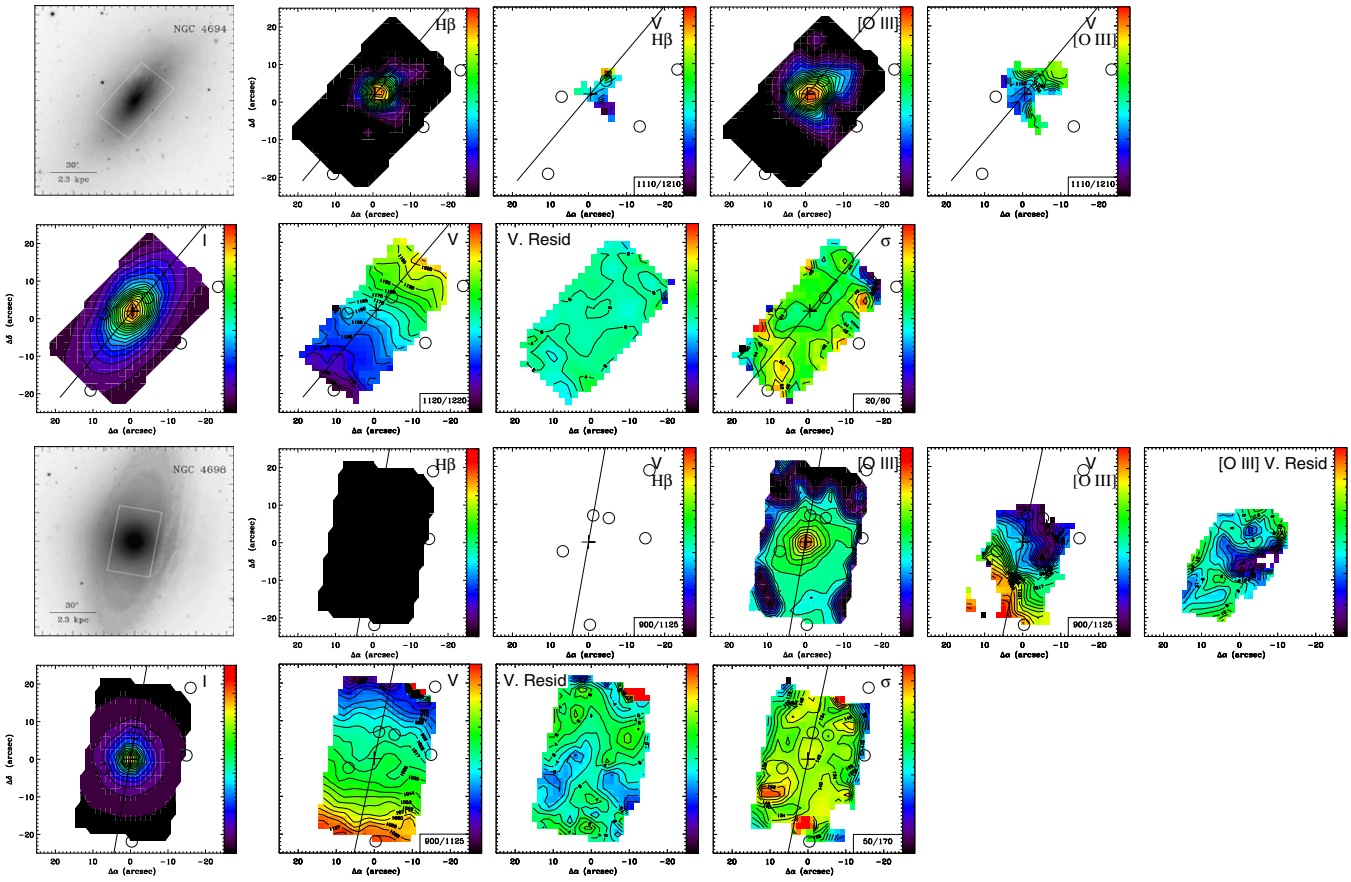


**Figure 6.** (Continued)

The stellar rotation curves span a range of amplitudes and a variety of shapes. There are galaxies with high stellar rotation velocities (e.g., NGC 4651 or NGC 4429) and those with extremely low stellar rotation velocities (e.g., NGC 4424, NGC 4351, or NGC 4606), and this difference reflects the difference in mass between the galaxies. However, there is also variety in the shapes of the stellar rotation curves for a given galaxy mass. Whereas some galaxies, such as NGC 4064, NGC 4580, and NGC 4651, display a monotonically rising stellar rotation curve over the entire array, others, such as NGC 4429, NGC 4450, and NGC 4457, exhibit a maximum within the inner 10″ indicating high central mass concentrations.

Stellar velocity dispersion profiles display behaviors as diverse as the stellar rotation curves. Some galaxies have high amplitudes in their central velocity dispersion, e.g., NGC 4429 with $\sigma \sim 200$ km s$^{-1}$. Others, such as NGC 4424 and NGC 4694, exhibit very small amplitudes ($\sigma \sim 50$ km s$^{-1}$). These differences are mostly due to galaxy mass. Galaxies such as NGC 4569, NGC 4651, and NGC 4450 exhibit centrally peaked $\sigma$ profiles that decrease outward, but other galaxies, such as NGC 4698, NGC 4694, and NGC 4606, have essentially flat velocity dispersion profiles.

Figure 10 shows the correlation between the absolute $H$ magnitude, derived using apparent $H$ magnitudes (Gavazzi et al. 1999) and our stellar-kinematics-based distances (Cortés et al. 2008), and the maximum stellar velocity rotation, and the central stellar velocity dispersion. As expected from the Tully–Fisher and Faber-Jackson relations, the variations in $V_{\rm max}$ and $\sigma$ among the sample galaxies are due predominantly to galaxy mass.

Finally, the $V/\sigma$ ratios show that some galaxies (e.g., NGC 4651, NGC 4569, or NGC 4580) are largely supported by rotation ($V/\sigma \geqslant 1$ at $R \geqslant 0.10\,R_{25}$, where $R_{25}$ is the radius where the surface brightness has a value of 25 mag arcsec$^{-1}$), but others such as NGC 4424, NGC 4429, and NGC 4698 have $V/\sigma < 1$ over the entire array, and are therefore supported by random motions as far as we measure.

## 5. KINEMATIC FEATURES AND PECULIARITIES

While $V$ and $\sigma$ are fundamental measures of galaxy support, there are important kinematic features of galaxies that are not captured by the radial variations of $V$ and $\sigma$. These include differences between photometric and kinematic axes, changes in kinematic position angle with radius (Figure 11), differences in stellar and gas kinematics, and kinematically distinct components. For example, the presence of kinematic misalignments in galaxies are often used to assess the frequency of triaxiality by measuring differences between the photometric and the stellar kinematics major axes, or to determine the occurrence of accretion events by measuring the misalignment between the kinematics of the stellar and gaseous components (e.g., Falcón–Barroso et al. 2006). Changes in position angle may indicate a bar (Cortés et al. 2006).

Many things can cause differences in stellar and gas kinematics. Some of these are normal features of galaxies that do not directly indicate any galaxy interaction, such as nuclear outflows, bar or spiral arm streaming motions, and a different balance of support between rotational and random motions. In this paper, we are more interested in those things which indicate some type of interaction, such as gas lying in a tilted plane with respect to the stars due to accretion events, or ram pressure disturbing the gas but not the stars.

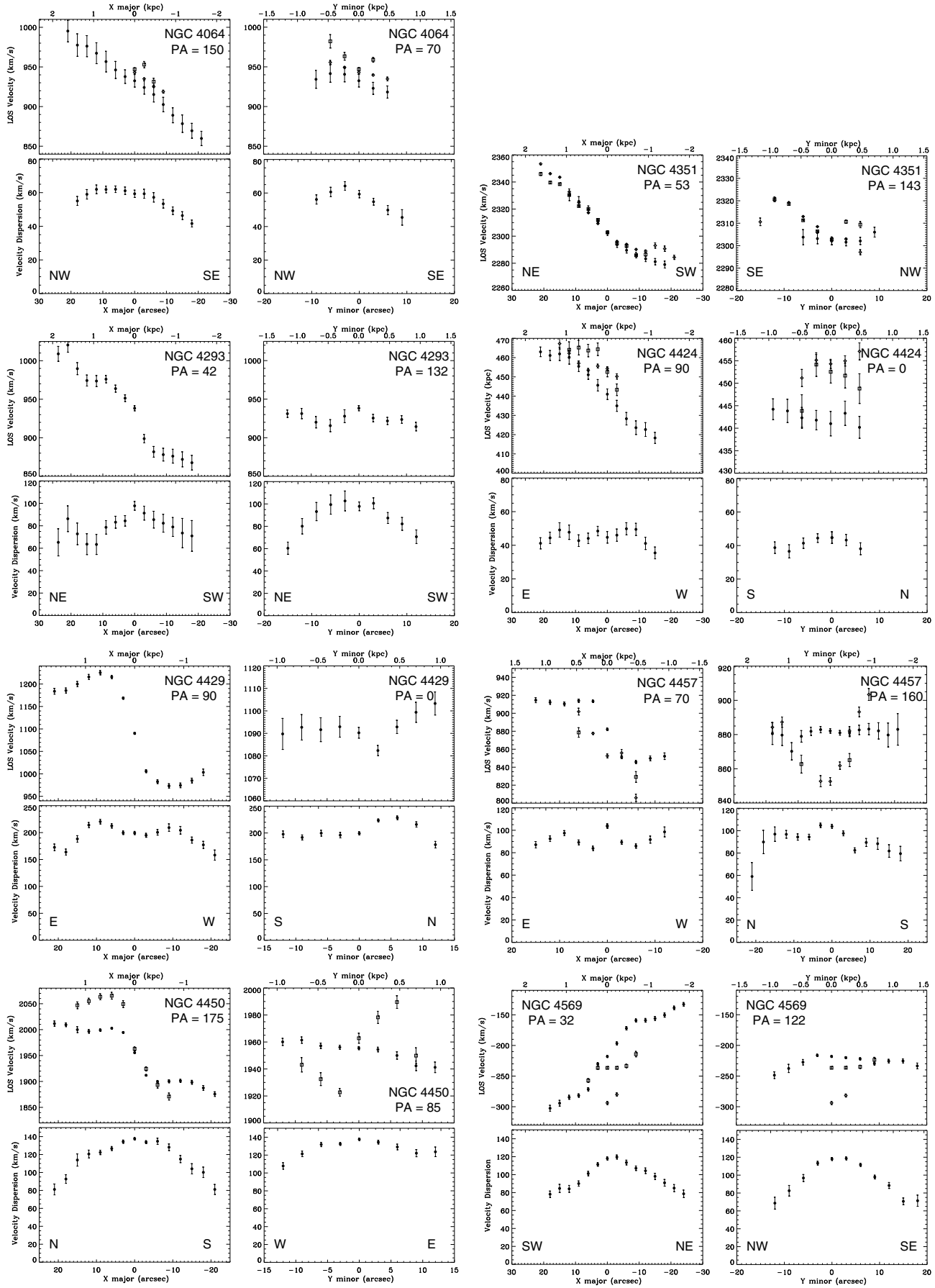


**Figure 7.** Stellar and ionized gas kinematics along kinematical major and minor axes. Solid symbols represent stellar kinematics, H$\beta$ gas kinematics is represented by diamonds, and [O III] gas kinematics is represented by squares.

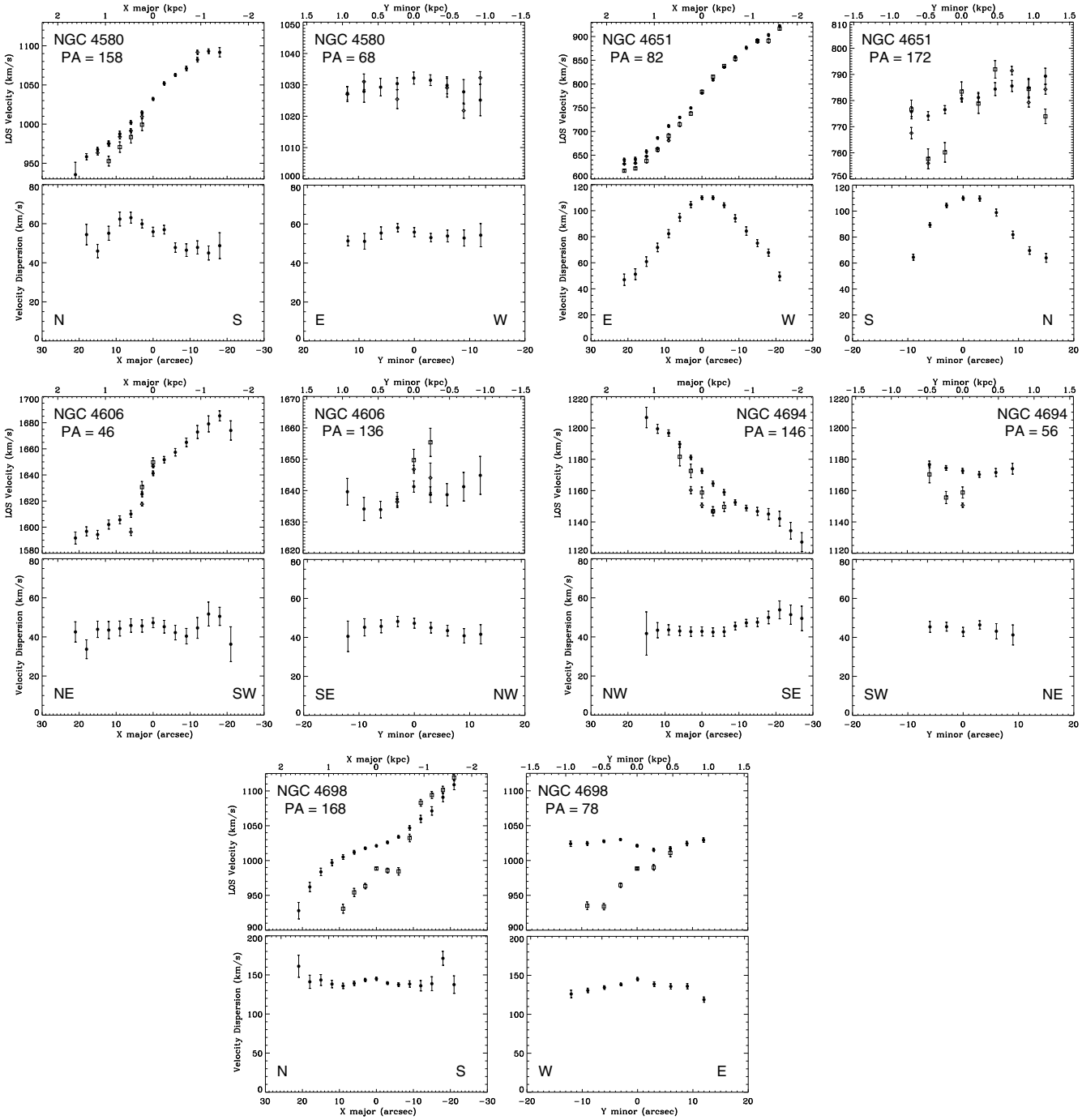


**Figure 7.** (Continued)

Kinematically distinct components are of interest since they can indicate a past merger or accretion event. Four of our sample galaxies display signatures of kinematically distinct components, with the most remarkable cases in NGC 4429 and NGC 4698.

### *5.1. Stellar Kinematics Misalignments*

Both photometric and kinematic position angles can vary with radius. These radial changes provide important information concerning the structure and history of the galaxy and need to be considered when comparing photometric and kinematic position angles. In our sample, there are several galaxies that exhibit significant radial changes in photometric or kinematic position angles. For example, in NGC 4293 and NGC 4569, there are photometric position angle changes from the inner to the outer galaxy associated with apparent warping of the outer disks. To handle this complexity, we will compare the stellar kinematic position angles with photometric PAs measured at more than one radius. In NGC 4064 and NGC 4450, the stellar kinematic PA varies with radius (Figure 11) due to the effect of stellar bars whose relative importance varies with radius. We will discuss these cases in the text.

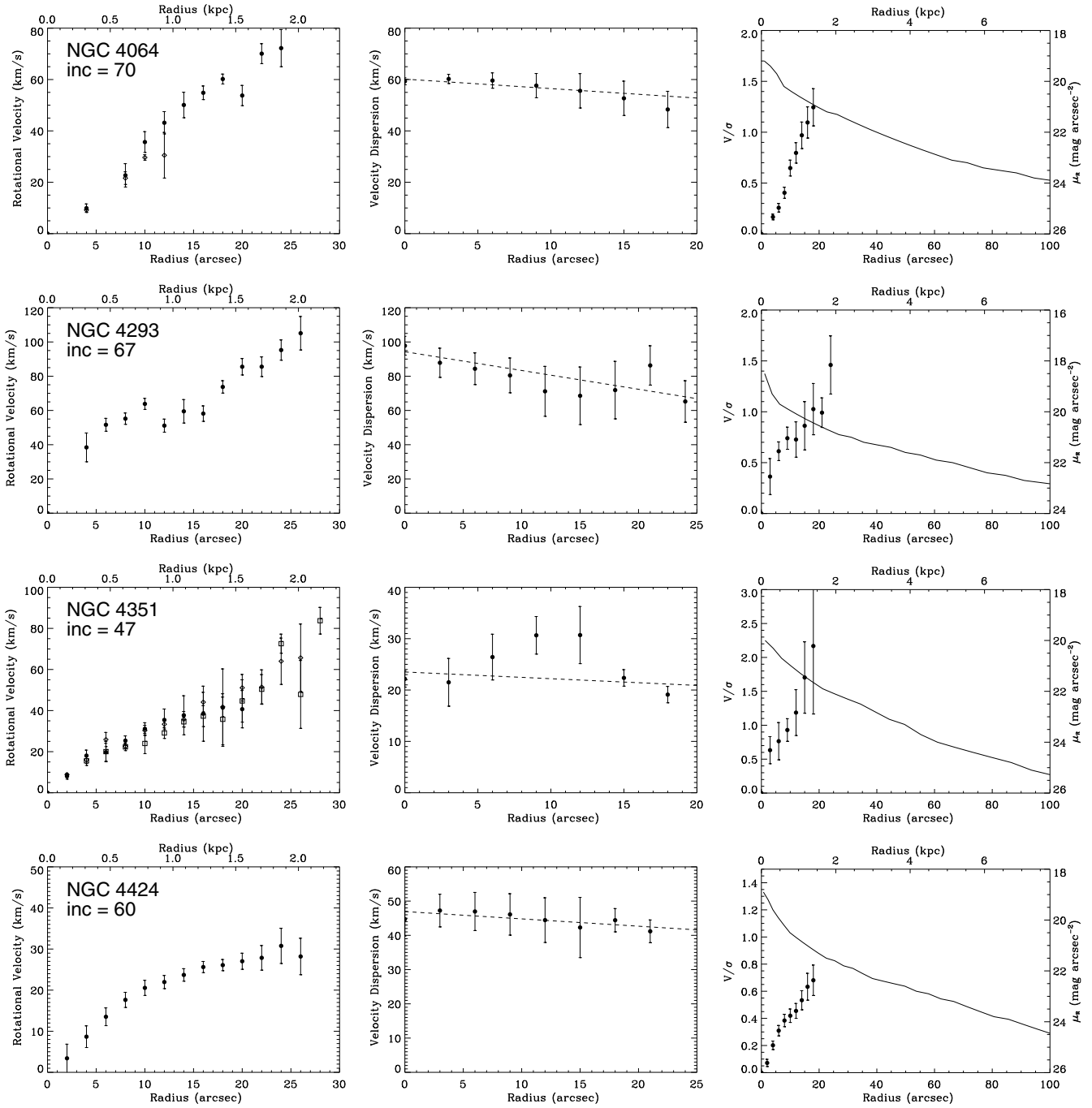


**Figure 8.** Stellar and ionized gas rotation curves, velocity dispersion profiles, and $V/\sigma$ ratios. Left panels: stellar and ionized gas rotation curves. Solid symbols represent stellar velocities, diamonds represent H$\beta$ velocities, and squares represent [O III] velocities. Middle panels: mean stellar velocity dispersion profiles. Solid symbols represent stellar velocity dispersion, and dashed lines represent the best linear profile fitted to stellar velocity dispersions. Right panels: ratio between the stellar rotation curve and the stellar velocity dispersion profile. Open and solid symbols represent different sides of the galaxy. The solid line represents the *R*-band radial light profile from Koopmann et al. (2001).

We define the inner galaxy stellar kinematics position angle $PA_{kin}$ as the mean of the kinematic position angles $\phi$ (see Section 3.3), within the inner 25″, i.e.,

$$PA_{kin} = \langle \phi \rangle \, . \tag{4}$$

To help deal with the fact that in some of our galaxies the outer galaxy is disturbed or tilted with respect to the inner galaxy, we compare the inner galaxy stellar kinematics PA (SKPA) with the photometric PA measured at two different radii, an outer radius of $1.0R_{25}$, $PA_{outer}$ and an intermediate radius of $0.5R_{25}$, $PA_{inter}$. For the photometric position angle determinations, we use photometry from our own optical images (J. R. Cortés et al. in preparation).

The kinematical misalignments $\Psi_{outer}$ and $\Psi_{inter}$ are defined as (Cappellari et al. 2007)

$$\Psi_{outer} = |PA_{kin} - PA_{outer}|, \tag{5}$$

$$\Psi_{inter} = |PA_{kin} - PA_{inter}|, \tag{6}$$

and are given for all of the galaxies in our sample in Table 4.

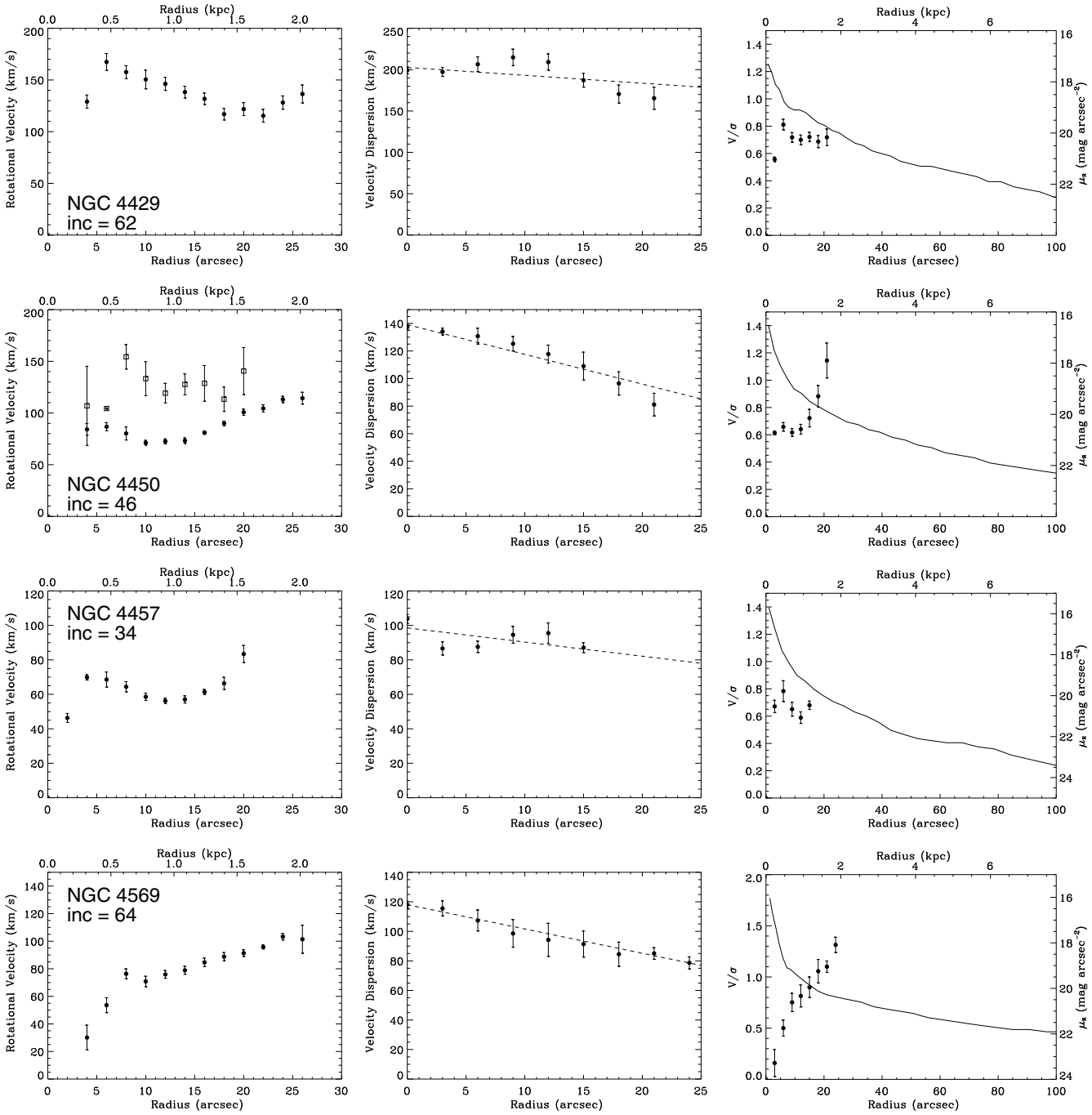


**Figure 8.** (Continued)

For six sample galaxies, both $\Psi_{\rm outer}$ and $\Psi_{\rm inter} \leqslant 7^{\circ}$ and the degree of misalignment is small. For these galaxies the inner stellar kinematics exhibit rotational motions consistent with stellar bodies flattened by rotation. This set includes several galaxies that are nonetheless clearly disturbed: NGC 4424, NGC 4606, and NGC 4694.

The other seven sample galaxies have PA differences of $\geqslant 10^{\circ}$ for $\Psi_{\rm outer}$, $\Psi_{\rm inter}$, or both. These galaxies can be grouped into those with bars or suspected bars (NGC 4064, NGC 4450, and NGC 4293), those with irregular or disturbed stellar velocity fields (NGC 4351 and NGC 4569), and those with photometric features not aligned with most of the galaxy (NGC 4429 and NGC 4651).

In both NGC 4064 and NGC 4450, the stellar kinematic PA, $\phi$, varies with radius (Figure 11), which we think is due to strong bar streaming motions whose magnitude changes with radius. NGC 4064 exhibits a clear difference between the kinematic PA and optical PA angle of about 50° in the inner 10″, a difference which is reduced to 10° at the end of the array ($r = 22''$). This produces an S-type shape in the isovelocity contours. This galaxy exhibits photometric and kinematical evidence of a bar (Cortés et al. 2006) that skews the isovelocity contours parallel to the major axis of the bar (Athanassoula 1992; Vauterin & Dejonghe 1997). Thus, it seems clear that the presence of the bar is the cause of the large differences between the kinematical and optical PAs in NGC 4064.

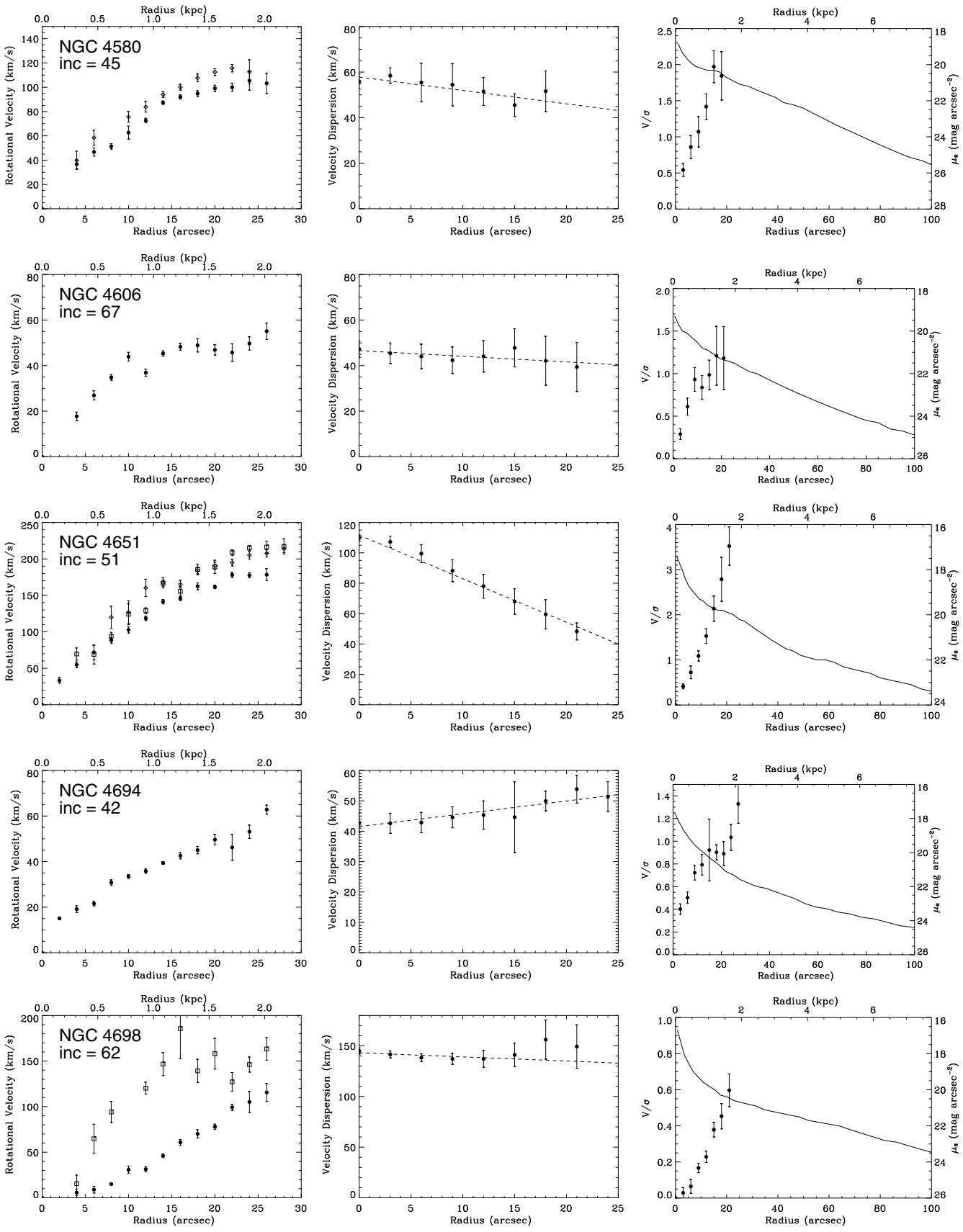


**Figure 8.** (Continued)

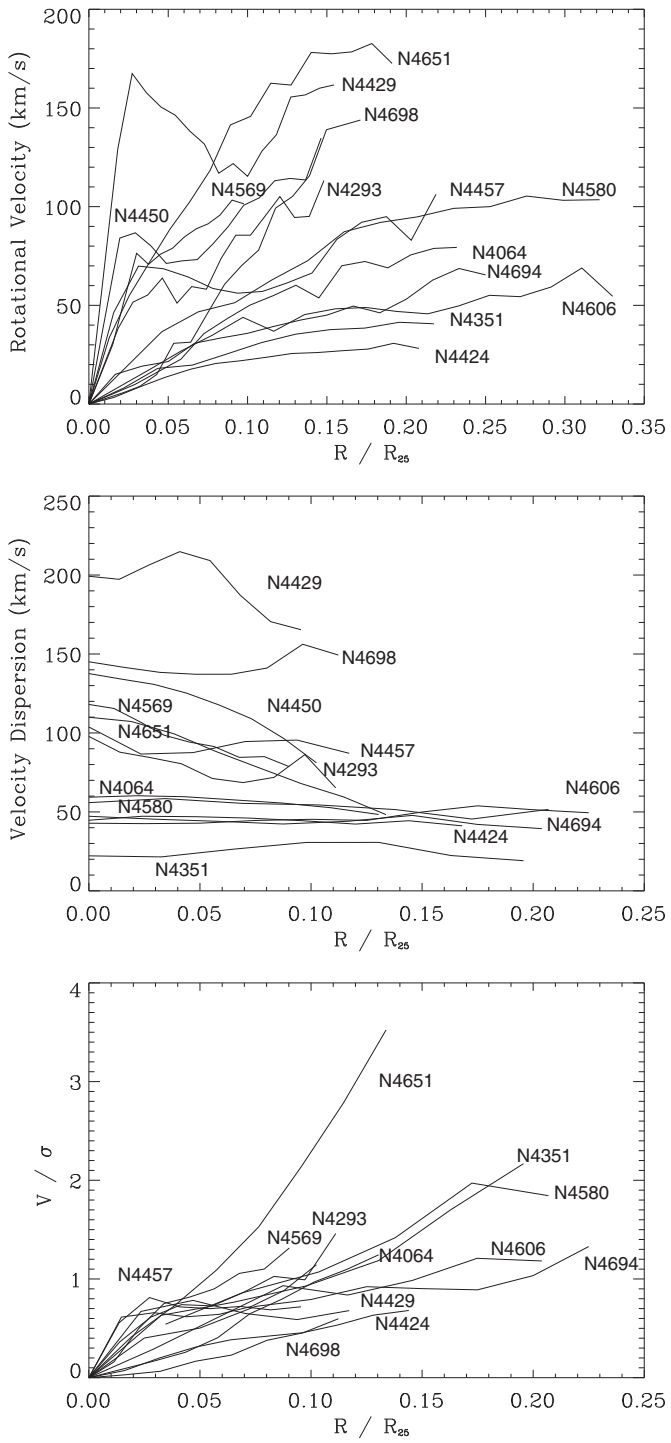


**Figure 9.** Stellar mean rotation curves, mean velocity dispersion profiles, and mean $V/\sigma$ ratios. All sample galaxies are represented in these plots. Galactocentric radii for sample galaxies were normalized by $R_{25}$ (Koopmann et al. 2001), defined as the radius where the surface brightness of the galaxy is 25 mag arcsec$^{-1}$ in the $R$ band.

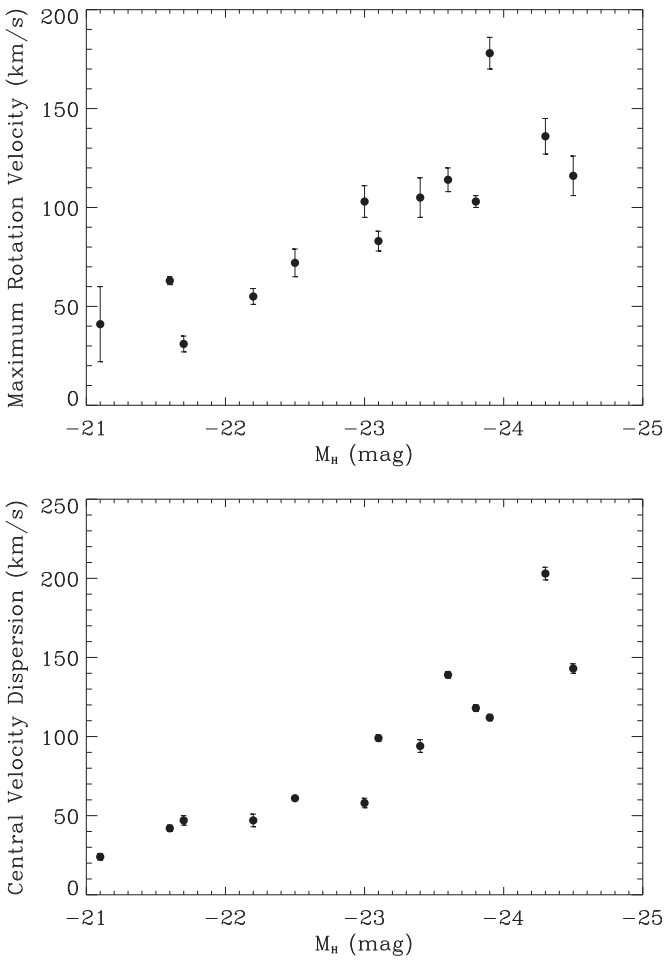


**Figure 10.** Maximum stellar velocity amplitudes and galaxy absolute magnitudes. The maximum stellar velocities are correlated with the brightness of the galaxies. Top: maximum stellar rotation velocities and $M_H$ magnitudes. Bottom: central stellar velocity dispersion and $M_H$ magnitudes. Velocities appear clearly correlated with $M_H$, indicating that the amplitude differences are due to differences in mass.

NGC 4450 seems similar but less extreme, probably because it has a larger bulge. While $\Psi_{\rm outer}$ and $\Psi_{\rm inter}$ differ significantly from zero, this is because the stellar kinematic position angle varies with radius and $\Psi$ values are calculated from the mean inner stellar kinematic PA. In the central 10″, it agrees well with the photometric PA of 175° in the outer galaxy. However, at $r \sim 15$–25″, the stellar kinematic PA is closer to 160°. This probably reflects a change from the inner bulge-dominated region to the bar-dominated region at larger radius.

In NGC 4293, the mean stellar kinematic PA is very different from the photometric PAs, and the reason is not clear. The outer stellar disk is tilted with respect to the inner disk, indicating a gravitational interaction, but the stellar kinematic position angle shows a very large difference of $\Psi_{\rm inter} = 35°$ with respect to the photometric PA at both intermediate and small radii (see the Appendix). There is no clear photometric evidence of a bar, although we cannot rule out a bar extended largely along the line of sight. Moreover, the stellar kinematic major and minor axes are largely perpendicular, and the velocity field does not exhibit the characteristic S-type shape which is expected in a barred galaxy, so there is also no clear kinematic evidence of a bar. A bar that is extended largely along the line of sight may be the reason for the large PA differences in NGC 4293, although other explanations are possible.

In NGC 4651, $\Psi_{\rm outer} = 10°$ but $\Psi_{\rm inter}$ is small because the outer disk is clearly disturbed, whereas the inner galaxy is much more regular and appears as a normal spiral galaxy. The outer galaxy contains a stellar tail and shells, and a disturbed outer H I distribution that appears warped (Chung et al. 2009), probably due to a minor merger. In NGC 4429, the stellar kinematic PA agrees with the photometric PA in both the inner galaxy

($r \leqslant 25''$) and the outer galaxy, but differs by 10° with respect to the photometric PA at intermediate radii. This is near the stellar ring at $r \sim 80''$, which seems tilted with respect to the rest of the galaxy.

In NGC 4569, $\Psi_{\rm inter} = 13° \pm 6°$, which is moderately large. Whereas $\Psi_{\rm outer}$ is smaller, this is due to the outer disk being tilted with respect to the inner disk, and it does not explain the apparent difference between stellar and photometric PAs in the inner galaxy. The inner stellar velocity field is somewhat irregular, possibly due to dust. The velocity field on the SE side of the major axis suggests a stellar kinematic PA closer to the photometric PA of the inner galaxy, whereas the NW side, which appears dustier, shows a greater difference.

In NGC 4351, the stellar velocity field is irregular and there are large values of $\Psi$. Both features may reflect disturbed central stellar kinematics. The outer isovelocity contours are curved toward the SW, suggesting disturbed stellar motions. While the stellar kinematic data on this fainter galaxy are somewhat noisy, similar features are observed in the gas isovelocity contours, suggesting that they may be real.

### 5.2. Discrepancies between Stellar and Ionized Gas Kinematics

Ionized gas velocity fields are generally more disturbed than the stellar velocity fields. The dissipative nature of the gas makes it more susceptible to many effects, including nuclear outflows and shocks triggered by bars or spiral arms. It also makes it a good tracer for hydrodynamical mechanisms such as ICM-ISM stripping, which might be revealed by certain differences between the stellar and gas kinematics. Moreover, the misalignment between the stellar and gas kinematics can be a signature of accretion events (e.g., Kannappan & Fabricant 2001).

Misalignments between stellar and gas kinematic position angles are found in NGC 4351, NGC 4450, and NGC 4698. In the case of NGC 4450, the misalignment is 25° with respect to the kinematic PA for [O III]. This is not observed by Chemin et al. (2006) in H$\alpha$ since the H$\alpha$ emission is weak in the center of NGC 4450 and the H$\alpha$ velocity field of Chemin is noisy. The center of NGC 4450 has been classified as a LINER (Ho et al. 2000), and accordingly its H$\beta$ emission is very weak and its [O III] emission is moderately strong. This misalignment could be due to the nuclear activity of this galaxy, although its [O III] velocity field seems to be consistent with rotation rather than an outflow. Alternatively, the gas might be located in a tilted plane with respect to the stars, which could be produced by an accretion event or minor merger.

NGC 4698 presents an [O III] velocity field with a kinematic PA different by 30° from the stars. This galaxy has been classified as a Seyfert 2 galaxy (Georgantopoulos & Zezas 2003), so its unusual ionized gas kinematics could be related to nuclear activity, but the [O III] velocity field is well ordered and seems to be largely consistent with rotation. A more likely explanation is that the gas distribution is non-planar, and the equilibrium plane of the gas gradually changes from larger radii, where the outer disk dominates the gravitational potential, to smaller radii, where the orthogonally rotating bulge dominates the potential.

In NGC 4351, the misalignment is about 10° and the galaxy is apparently lopsided (Rudnick et al. 2000), which could suggest a tidal interaction or minor merger. The galaxy has a nearby neighbor IC 3258 (separation ~80 kpc) with a mass of about half of the NGC 4351 mass, but the relative velocity with respect to NGC 4351 is about 2700 km s$^{-1}$, making the possibility of a strong tidal interaction between the galaxies unlikely. Moreover, the outer stellar disk seems undisturbed.

Alternatively, the bending of the outer ionized gas isovelocity contours in NGC 4351 could be a signature of ICM-ISM stripping. A similar bending is observed in NGC 4457, and both galaxies have gas kinematics and morphologies which could plausibly be caused by ram pressure (see Appendix).

NGC 4569 displays disturbed ionized gas velocity fields with a velocity gradient along the minor axis. The galaxy nucleus has been classified as a LINER (Keel 1996), and radio maps of NGC 4569 strongly suggest a nuclear outflow (Chyży et al. 2006). H$\alpha$ + [N II] imaging reveals a C-shaped filament resembling the edges of a cone near the minor axis in the SE, also suggestive of a nuclear outflow (J. D. P. Kenney et al., in preparation).

### 5.3. Kinematically Distinct Components

The existence of kinematically distinct components such as decoupled cores, cold stellar disks, or counter-rotating components in galaxies could be used as a good tracer of environmental interaction such as mergers or gas accretion. With the purpose of investigating such possibilities, we analyzed line-of-sight velocity distributions (LOSVD) by obtaining the cross-correlation function along the major and minor axes of the galaxies using the IRAF task FXCOR. This task has the advantage of visualizing LOSVD independent of the employed parameterization, which is not possible with pPXF since we were restricted to obtain $V_{\rm LOS}$ and $\sigma$ due to signal-to-noise limitations.

We estimate that with our data, we should be able to detect secondary kinematic components as weak as 20% of the primary component in those galaxies with higher signal-to-noise ratios and with a velocity difference of at least 60 km s$^{-1}$ ($\sim 2\Delta v$, with $\Delta v$ the velocity resolution). No signatures of counter-rotation, like the double peaked LOSVD as in NGC 4550 (Rubin et al. 1992; Rix et al. 1992), have been found, which could be an indication that galaxies like NGC 4550 are rare and created only under very special conditions.

Signatures of secondary kinematic components other than counter-rotation were found in NGC 4429, NGC 4450, NGC 4651, and possibly in NGC 4457. For NGC 4698, although signatures of an orthogonally rotating core are obvious from the stellar velocity field, we were unable to detect any apparent deviation or distinct kinematic components from the LOSVD profiles. NGC 4429, NGC 4450, and perhaps NGC 4457 exhibit tails in their LOSVDs toward the systemic velocity in their inner 10″. In the case of NGC 4429 and NGC 4450, these tails have an amplitude of about 20% of the amplitude of the main component. These tails are evidence of a two-component structure LOSVD (Rix & White 1992) within their inner 10″ with a hot slow-rotating component due to a bulge and rapidly rotating component. NGC 4651 also has tails extending toward the systemic velocity with an amplitude of 30% of the amplitude of the main component, but they are visible from $r = 10''$ to 20″ rather than in the center as for the other galaxies. This reveals the presence of a second hot, slow-rotating stellar component toward the outer parts of the galaxy that overlaps with the rapidly rotating main stellar component.

In spite of the low signal-to-noise ratio of the spectra (S/N < 60), we obtained higher moments ($h_3$ and $h_4$) of the LOSVD with pPXF, with the objective of investigating the nature of these asymmetries in the LOSVD. In bulge+disk systems, the shape of the LOSVD can be complicated (Scorza & Bender 1995), and even normal galaxies such as NGC 3898, NGC 7782,

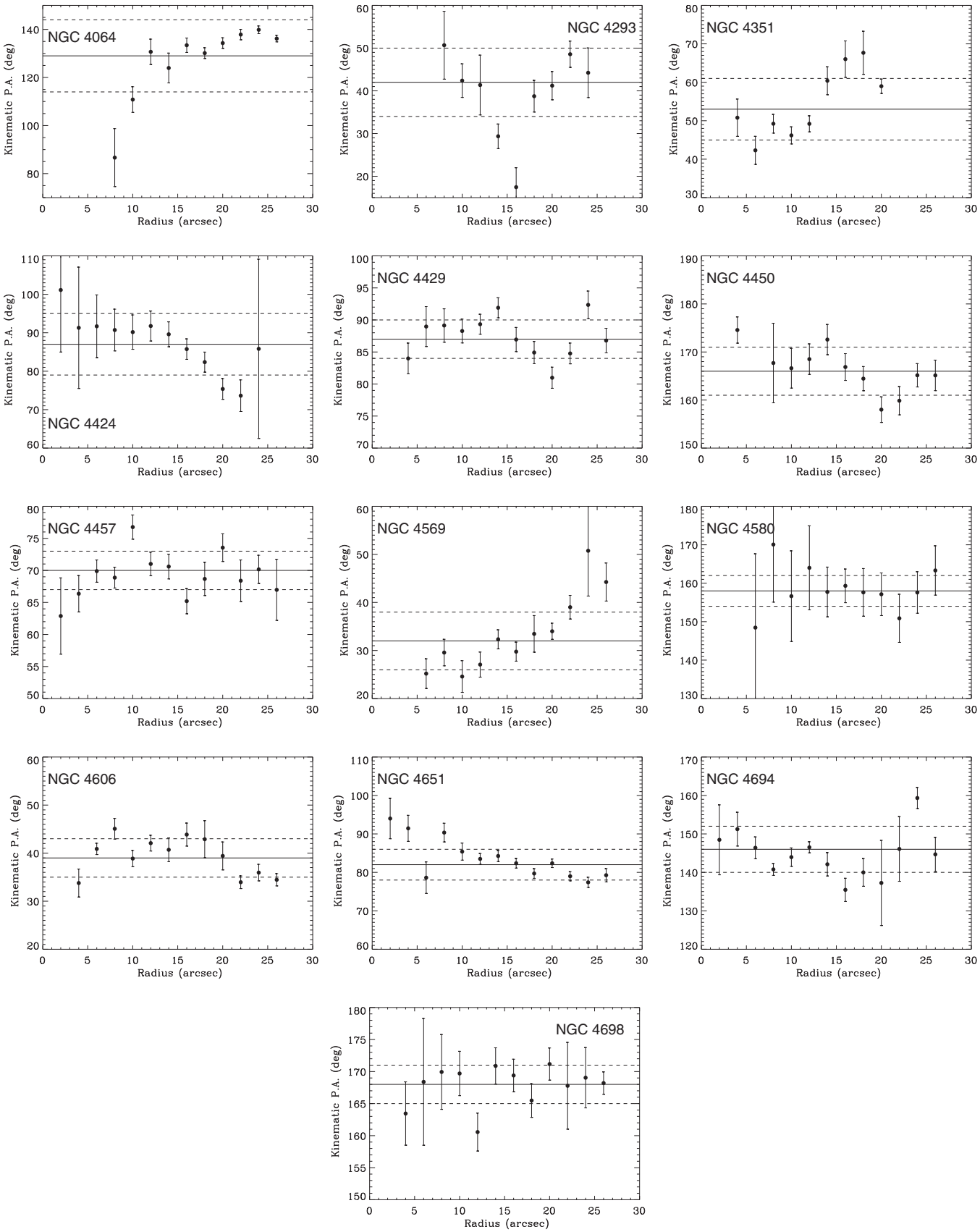


**Figure 11.** Stellar kinematic PA as function of radius for sample galaxies. Solid symbols represent the stellar kinematic position angles derived from the tilted ring models (Section 3.3). Solid lines represent the mean kinematic PA. The standard deviations of the mean are represented by dashed lines.

**Table 6**
Parameters Derived from the Stellar Velocity Dispersion Radial Profiles

| Name | $\sigma_0$ (km s$^{-1}$) | $\alpha$ (km s$^{-1}$ kpc$^{-1}$) |
|---|---|---|
| (1) | (2) | (3) |
| NGC 4064 | 61 ± 1 | −4.6 ± 2.3 |
| NGC 4293 | 94 ± 4 | −16.0 ± 5.8 |
| NGC 4351 | 24 ± 2 | −1.0 ± 1.0 |
| NGC 4424 | 47 ± 3 | −2.7 ± 2.7 |
| NGC 4429 | 203 ± 4 | −12.7 ± 5.1 |
| NGC 4450 | 139 ± 2 | −36.0 ± 4.9 |
| NGC 4457 | 99 ± 2 | −10.3 ± 2.6 |
| NGC 4569 | 118 ± 2 | −25.4 ± 2.9 |
| NGC 4580 | 58 ± 3 | −5.6 ± 2.8 |
| NGC 4606 | 47 ± 3 | −3.1 ± 3.1 |
| NGC 4651 | 112 ± 2 | −22.3 ± 1.5 |
| NGC 4694 | 42 ± 2 | 6.2 ± 3.1 |
| NGC 4698 | 143 ± 3 | −3.4 ± 3.4 |

**Notes.** (1) Galaxy name; (2) central velocity dispersion from a linear model for the dispersion profile; (3) velocity dispersion slope in km s$^{-1}$ kpc$^{-1}$.

and NGC 980 (Vega-Beltrán et al. 2001) have non-zero $h_3$ and $h_4$ moments. In our case, four moments maps for NGC 4429, NGC 4450, and NGC 4651 are shown in Figure 6. The most remarkable case is NGC 4429, which shows peaks at 10″ in the $V_{\rm LOS}$, a central dip in $\sigma$, signatures of an anti–correlation between $h_3$ and $V_{\rm LOS}$ in the inner 10″, and a positive $h_4$ in the inner 10″. All of these features, together with two-component structure LOSVD, are signatures of a cold stellar disk within the inner 10″. Even the low $V/\sigma$ ratio seems consistent with this scenario, since the bulge dominates the mass inside the central region. We calculate an upper limit on the circumnuclear disk mass as the dynamical mass inside $r = 10''$ where the rotation velocity peaks. This disk has a mass of less than one-fourth the mass of the galaxy inside $r = 25''$ where the kinematics and therefore the interior mass are dominated by the bulge.

Similar features are found in NGC 4450 and NGC 4457, although they are much weaker. The case of NGC 4651 exhibits an anti-correlation between $h_3$ and $V_{\rm los}$ toward the outer parts of the array that could be due to a slower rotating component. This is consistent with the presence of a tail toward the systemic velocity in LOSVD. NGC 4698 exhibits very low $h_3$ and $h_4$ values, even considering that it has an orthogonally rotating core. This is evidence of a relaxed system. Other galaxies of the sample do not show any apparent deviation from Gaussianity or tails in the LOSVD within the errors.

## 6. KINEMATICAL SUPPORT AND ANISOTROPY

### *6.1. Velocity Dispersion Profiles*

The stellar velocity dispersion profiles in stellar disks typically have exponential profiles with scale lengths about twice the scale length of the light from the disks (Bottema 1993). In our case, fitting an exponential profile could be misleading since our data are restricted to a region where the bulge is important. Instead, we fit a linear profile to our velocity dispersion profiles $\sigma(R)$ (Table 6; Figure 8) defined as

$$\sigma(R) = \sigma_0 + \alpha R, \quad (7)$$

where $\sigma_0$ is the central velocity dispersion and $\alpha$ is the slope of the velocity dispersion profile. We found that our galaxies display profiles with slopes ranging from roughly -36 km s$^{-1}$ kpc$^{-1}$ to 6 km s$^{-1}$ kpc$^{-1}$. The galaxies NGC 4293, 4450, 4569, and 4651 have $\sigma$ profiles with slopes steeper than −16 km s$^{-1}$ kpc$^{-1}$, but others have very small slopes with essentially flat profiles; these galaxies are NGC 4064, NGC 4351, NGC 4424, NGC 4606, NGC 4694 and NGC 4698. In Figure 12 (top panel), we show the concentration parameter $C_{30}$ (related to the bulge-disk ratio) with $\alpha$. We do not see a clear correlation with galaxies having steep or flat velocity dispersion profiles independent of how conspicuous their bulge are.

In the group of low $\alpha$ galaxies, NGC 4064, NGC 4424, NGC 4606, and NGC 4694 belong to the group of galaxies with "truncated/compact" profilesof H$\alpha$ (Koopmann & Kenney 2004; Section 2). NGC 4351 has been classified as "truncated/normal" but the low amplitude and flat dispersion profile could be due to the fact that the signal-to-noise ratio of the spectra in this galaxy is not enough to obtain reliable velocity dispersion measurements. Finally, NGC 4698 is a big anemic Sa galaxy with a clear secondary kinematic component. These objects also have the smallest $V/\sigma$ values within the central 20″ within the sample (Figure 9). What is the cause of these flat stellar velocity dispersion profiles?

One possible cause could be that we are measuring $\sigma$, even for the outermost observed position within the bulge-dominated region. We checked this using the available near-infrared photometry and light profile decomposition for NGC 4606, NGC 4694, and NGC 4698 (Gavazzi et al. 1996), and our own $R$-band light profile decomposition for NGC 4064 and NGC 4424 (Cortés et al. 2006). We found that for NGC 4064, NGC 4424, and NGC 4606, the bulge is much smaller than the size of the array (12″, 5″, and 9″, respectively), so the flat $\sigma$ extends farther than the bulge-dominated region. These are galaxies with less conspicuous bulges (low $C_{30}$, see Figure 12) and flat $\sigma$ profiles. In the cases of NGC 4694 and NGC 4698, the extension of the bulge is 16″ and 18″, respectively, so it could be that our measurements are still in the bulge-dominated region in these galaxies. In fact, these galaxies have $C_{30} > 0.5$, so their bulge is conspicuous.

Another possible explanation for the flat stellar velocity dispersion profiles and low $V/\sigma$ values is some kind of gravitational interaction. Mergers and tidal interactions tend to heat galaxy disks and increase the velocity dispersion (e.g., Bendo & Barnes 2000). Mergers simulations (Bendo & Barnes 2000) show that direct encounters of disk galaxies with mass ratios of 3:1 can produce remnants with flat velocity dispersion profiles, slowly rising stellar rotation curves, and $V/\sigma < 1$ in the inner 20% of the optical radii. NGC 4424 and NGC 4698 have remarkably low $V/\sigma$ ratios at radii where the disk starts to be important (0.3 and 0.5 respectively). In the case of NGC 4698, the existence of an orthogonally rotating core clearly indicates that this galaxy is the result of a merger. The optical morphology of NGC 4424 has features that suggest an intermediate-mass ratio merger (Kenney et al. 1996, Cortés et al. 2006). The fact that $V/\sigma$ is remarkably low and flat is consistent with the merger scenario. With its small bulge, disk-like morphology, and elliptical-like kinematics, NGC 4424 is likely an intermediate mass-ratio merger (Bournaud et al. 2004; Cortés et al. 2006).

NGC 4606 and NGC 4694 exhibit non-elliptical isophotes (J. R. Cortés et al., in preparation), slowly rising rotation curves, and low $V/\sigma$ ratios that resemble the kinematics found in the Bendo & Barnes prolate 3:1 merger remnants. On the other hand, NGC 4606 has a close companion NGC 4607 ($d \sim 17$ kpc, and $\Delta v = 593$ km s$^{-1}$), which could disturb this galaxy and produce a flat $\sigma$ profile. The two galaxies have

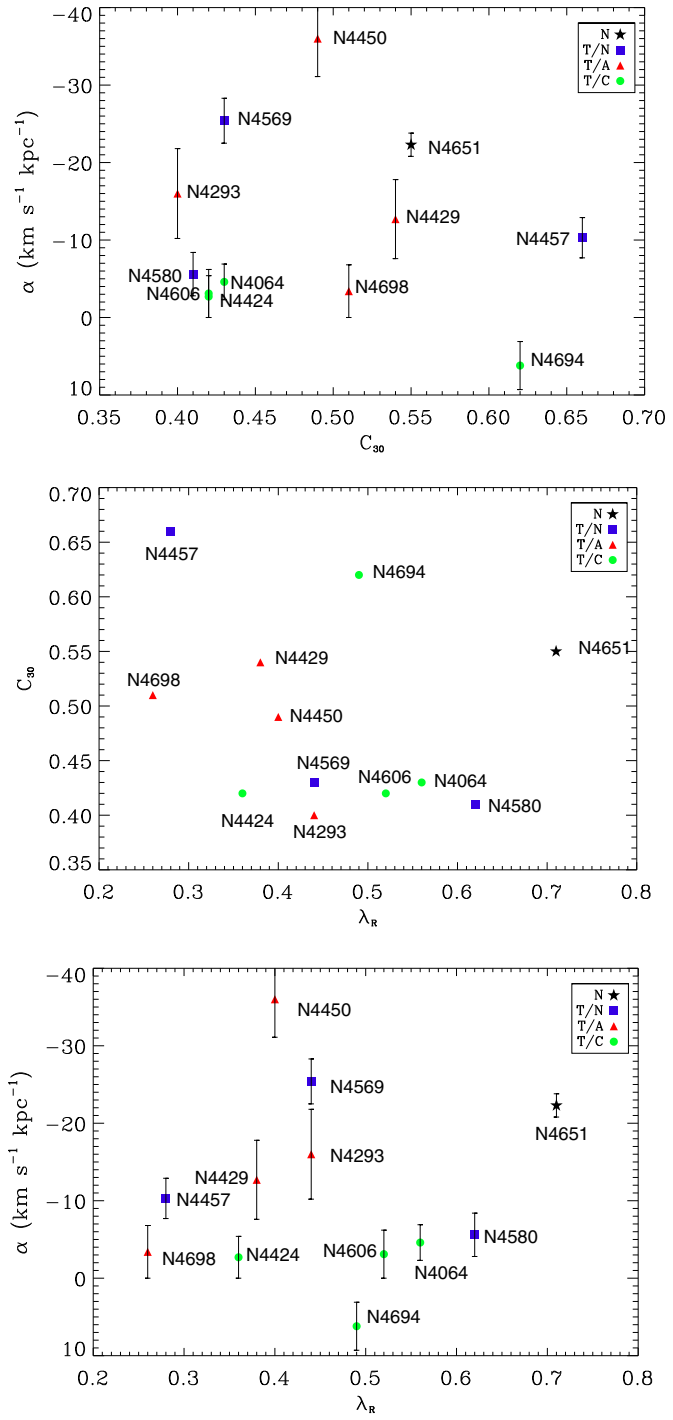


**Figure 12.** $\lambda_R$ parameter, concentration ($C_{30}$), and velocity dispersion slope $\alpha$. Top panel: $C_{30}$ and $\alpha$. Middle panel: $C_{30}$ and $\lambda_R$. Bottom panel: $\lambda_R$ and $\alpha$. Symbols represent different star formation classifications: black stars = Normal (N), red triangles = Truncated/Anemic (T/A), blue squares = Truncated/Normal (T/N), and green circles = Truncated/Compact (T/C). Here, we see that galaxies with star formation classes T/A and T/N span a wide range of $\alpha$ values, but T/A tends to have low $\lambda_R$ (<0.45). T/C galaxies have a nearly flat velocity dispersion profiles.

similar luminosities and masses. NGC 4607 looks less disturbed than NGC 4606, which might be inconsistent with a strong tidal interaction between these two galaxies, although if the interaction is prograde for one galaxy (e.g., NGC 4606) and retrograde for the other (e.g., NGC 4607), then it is possible to have one companion significantly more disturbed than the other. In any case, NGC 4606 has clearly experienced a recent gravitational disturbance.

Finally, the case of NGC 4694 is less compelling since the bulge is about the size of the DensePak array, and the $V/\sigma$ ratio becomes ~1 at end of the bulge-dominated region. This galaxy has a disturbed H I tail connecting with a close dwarf companion VCC 2062, indicating a clear ongoing gravitational interaction (van Driel & van Woerden 1989; Chung et al. 2007; Chung et al. 2009). The velocity dispersion actually increases slightly with increasing radius, a trend not observed in any other galaxy. We speculate that this could be the result of recent star formation in the center of the galaxy, which creates a low-dispersion circumnuclear disk.

### 6.2. Kinematical Support

In order to understand the kinematical support of sample galaxies, we made use of the $\lambda_R$ parameter (Emsellem et al. 2007), which is a practical way to quantify the global velocity structure of galaxies using the 2D spatial information provided by the integral-field units and for quantifying the specific angular momentum. This dimensionless parameter can be measured via 2D spectroscopy (Emsellem et al. 2007) as

$$\lambda_R = \frac{\sum_{i=1}^{N} F_i R_i |V_i|}{\sum_{i=1}^{N} F_i R_i \sqrt{V_i^2 + \sigma_i^2}}, \quad (8)$$

where $N$ is the number of fibers in the DensePak array, $F_i$ is the flux inside the $i$th DensePak fiber, $R_i$ its distance to the center, and $V_i$ and $\sigma_i$ are the corresponding mean stellar velocity and velocity dispersion. The parameter $\lambda_R$ is close to unity when the mean rotation ($V$) dominates. On the contrary, $\lambda_R$ goes to zero if the mean velocity dispersion ($\sigma$) dominates.

The values of $\lambda_R$ for sample galaxies are displayed in Table 7. Following the kinematical classification introduced by Emsellem et al. (2007) and refined by the ATLAS$^{3D}$ project (Emsellem et al. 2011), all of our galaxies can be classified as fast rotators with their location in the $\lambda_R$—$\epsilon$ diagram (Figures 13 and 14), above the so-called "green line" (Figure 14) defined as $\lambda_R = 0.31\sqrt{\epsilon}$ (Emsellem et al. 2011), as expected for disk galaxies. In fact, all of our galaxies show nearly regular and symmetric velocity fields consistent with being fast rotators. NGC 4698 has the smallest $\lambda_R = 0.26$, and the highest corresponds to NGC 4651 with $\lambda_R = 0.71$. Also, most of our sample galaxies are located below the location expected for an isotropic rotator (Figure 14, black line), so it is clear that they cannot be considered simple isotropic oblate rotators as expected.

In Figure 12 (middle panel), we display $\lambda_R$ versus the concentration parameter $C_{30}$, which is a measure of the bulge-to-disk ratio. We see that galaxies with low $\lambda_R$ tend to have a high $C_{30}$ value, although the sample is too small to derive further conclusions. In the case of the relationship between $\lambda_R$ and the slope of the velocity dispersion profile $\alpha$ (Figure 12, bottom panel), we see that galaxies classified as [T/A], [T/N], and [N] can span a wide range of $\alpha$ independent of the value of $\lambda_R$. In the case of the [T/C] galaxies, they have flat velocity dispersion profiles in spite of their amount of rotational support. The possibility of this being caused by 3:1 or higher mass-ratio mergers is explored in the following section.

## 7. COMPARISON WITH SIMULATIONS

$N$-body (e.g., Bendo & Barnes 2000; Jesseit et al. 2007) and hydrodynamic simulations (e.g., Kronberger et al. 2007;

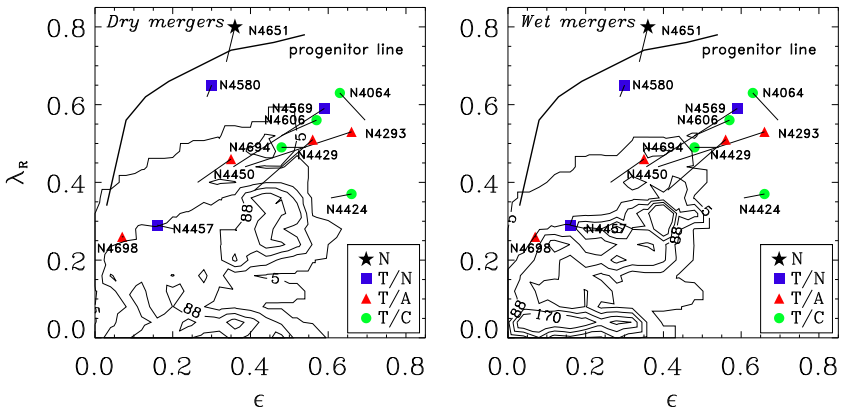


**Figure 13.** Distribution of merger remnants with mass ratios of 3:1 to 1:1 in the $\lambda_R$–$\epsilon$ plane. Symbols represent different star formation classifications: black stars = Normal (N), red triangles = Truncated/Anemic (T/A), blue squares = Truncated/Normal (T/N), and green circles = Truncated/Compact (T/C). Solid lines connect the uncorrected (observed) and corrected (to $R_{1/2}$) values of $\epsilon$ and $\lambda_R$; the symbols are plotted at the corrected values. Contours represent the distribution of 1:1 and 3:1 merger remnants from Jesseit et al. (2009) simulations. The progenitor galaxy location is indicated as a thick line. The left panel displays collisionless mergers (dry) and the right panel displays mergers remnants that formed with gas (wet). Only two galaxies are close to the progenitor line (NGC 4580 and NGC 4651), and so have not experienced any major gravitational disturbance. The remaining galaxies are dynamically warm or lukewarm, and thus have experienced significant gravitational disturbances.

**Table 7**
Measured and Modeled Parameters: $\sqrt{\langle V^2/\sigma^2\rangle}$, $\lambda_R$, and Ellipticity

| Name | $\sqrt{\langle V^2/\sigma^2\rangle}$ | $\lambda_R$ | $\epsilon$ | $R_{1/2}$ | $\lambda_R$(iso) | $\lambda_{R_{1/2}}$(iso) | $k$ | $\lambda_{R_{1/2}}$ | $\langle\epsilon\rangle_{1/2}$ |
|---|---|---|---|---|---|---|---|---|---|
| (1) | (2) | (3) | (4) | (5) | (6) | (7) | (8) | (9) | (10) |
| NGC 4064 | $0.61 \pm 0.05$ | 0.56 | 0.69 | 37 | 0.69 | 0.75 | 0.81 | 0.61 | 0.63 |
| NGC 4293 | $0.47 \pm 0.08$ | 0.44 | 0.39 | 67 | 0.76 | 0.91 | 0.58 | 0.53 | 0.66 |
| NGC 4424 | $0.37 \pm 0.09$ | 0.36 | 0.61 | 39 | 0.79 | 0.82 | 0.46 | 0.37 | 0.66 |
| NGC 4429 | $0.41 \pm 0.02$ | 0.38 | 0.41 | 61 | 0.63 | 0.85 | 0.60 | 0.51 | 0.56 |
| NGC 4450 | $0.35 \pm 0.03$ | 0.40 | 0.26 | 53 | 0.72 | 0.82 | 0.56 | 0.46 | 0.35 |
| NGC 4457 | $0.31 \pm 0.08$ | 0.28 | 0.20 | 26 | 0.61 | 0.62 | 0.46 | 0.29 | 0.16 |
| NGC 4569 | $0.43 \pm 0.03$ | 0.44 | 0.36 | 95 | 0.66 | 0.89 | 0.66 | 0.59 | 0.59 |
| NGC 4580 | $0.76 \pm 0.11$ | 0.62 | 0.29 | 29 | 0.70 | 0.73 | 0.89 | 0.65 | 0.30 |
| NGC 4606 | $0.74 \pm 0.08$ | 0.52 | 0.48 | 34 | 0.63 | 0.67 | 0.83 | 0.56 | 0.57 |
| NGC 4651 | $0.94 \pm 0.04$ | 0.71 | 0.34 | 36 | 0.60 | 0.68 | 1.18 | 0.80 | 0.36 |
| NGC 4694 | $0.68 \pm 0.08$ | 0.49 | 0.54 | 27 | 0.90 | 0.90 | 0.55 | 0.49 | 0.48 |
| NGC 4698 | $0.28 \pm 0.03$ | 0.26 | 0.07 | ... | ... | ... | ... | ... | ... |

**Notes.** (1) Galaxy name; (2) luminosity-weighted $V/\sigma$; (3) $\lambda_R$ measured over the entire array (25″); (4) ellipticity estimated within the inner 25″ from 2MASS $H$-band images (Jarrett et al. 2003); (5) half-light radius in arcseconds; (6) $\lambda_{Riso}$ over the inner 25″ derived from isotropic two-integral dynamical models (Cortés et al. 2008); (7) $\lambda_{R_{1/2}iso}$ over the inner $R_{1/2}$ derived from isotropic two-integral dynamical models (Cortés et al. 2008); (8) $k$, ratio between observed $\lambda_R$ measured over the inner 25″ to $\lambda_R$ within the inner 25″ derived from isotropic two-integral dynamical models; (9) $\lambda_R$ estimated in the inner $R_{1/2}$ from two-integral dynamical models corrected by isotropy; (10) luminosity-weighted ellipticity within the inner $R_{1/2}$.

Kronberger et al. 2008) have started to produce 2D kinematics that can be compared with the observed velocity and velocity dispersion fields of galaxies. In order to search for clues about what physical processes have acted on these galaxies, and which ones are driving galaxy evolution, we compare our observed kinematics with the results of simulations of gravitational interactions (i.e., mergers and tidal encounters) and ICM–ISM stripping.

### 7.1. Gravitational Interactions

Gravitational interactions include mergers and non-merging gravitational encounters. In clusters, most of the non-merging gravitational encounters will be high-velocity encounters, sometimes called harassment. Slow encounters can also be important, since gravitationally bound galaxies may interact and later become unbound through gravitational interaction with another object. It can be hard to distinguish between minor mergers, low-velocity encounters, and high-velocity encounters without detailed information, since many of their impacts are similar. While all have been simulated, we are not aware of any suite of simulations that has included the variety of gravitational interactions and attempted to distinguish between them. In the following, we compare the dynamical heating and kinematic properties of our Virgo sample mostly with merger simulations, since the results of such simulations exist in a form that can be easily compared with our data. We discuss simulation results from non-merging gravitational encounters where possible.

#### 7.1.1. Dynamical Heating of Sample Galaxies

The results of the SAURON and ATLAS$^{3D}$ projects show that the possible merger origin of galaxies can be assessed by comparing the location of a galaxy sample (Figure 13) in

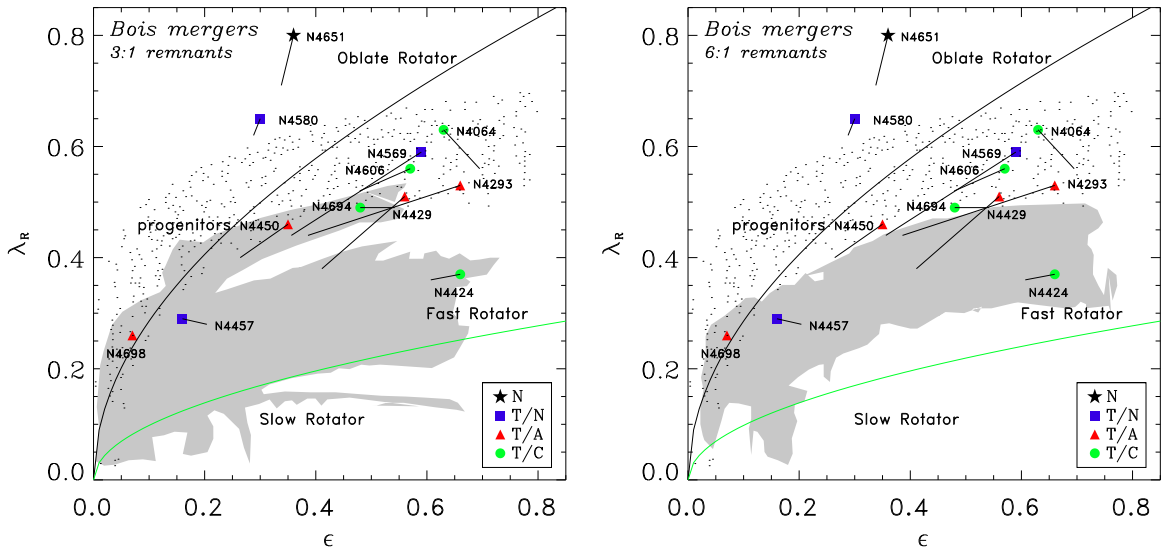


**Figure 14.** Sample galaxies in the $\lambda_R$–$\epsilon$ plane. Symbols represent different star formation classifications: black stars = Normal (N), red triangles = Truncated/Anemic (T/A), blue squares = Truncated/Normal (T/N), and green circles = Truncated/Compact (T/C). Solid lines connect the uncorrected (observed) and corrected (to $R_{1/2}$) values of $\epsilon$ and $\lambda_R$; the symbols are plotted at the corrected values. Black solid line represents the location of oblate rotators, the green line represents the boundary between slow and fast rotators. Black dots represent spiral-like progenitor galaxies from the Bois et al. (2011) simulations. The gray shading covers the region of the Bois et al. (2011) merger remnants. The left panel displays the merger remnant locations with a mass ratio of 3:1. Right panel displays the merger remnant locations with a mass ratio of 6:1.

the $\lambda_R$–$\epsilon$ plane measured within the effective radius, with the location for merger remnants given by simulations (e.g., Jesseit et al. 2009; Bois et al. 2011). Our observations reach a radius of 25″, which in most cases is less than the half-light radius (Table 7). Thus, in order to carry out this comparison, it is necessary to estimate $\lambda_R$ and the luminosity-weighted ellipticity $\epsilon$ at half-light radius (equivalent to the effective radius for spiral galaxies). To perform this estimation, we made use of our *R*-band light profiles and two-integral dynamical models (Cortés et al. 2008) as follows.

1. We estimated the half-light radius $R_{1/2}$ from our *R*-band light profiles.
2. We derived $\lambda_R$ at $R = 25''$ and at $R = R_{1/2}$ form our Jeans isotropic models as it is described by Equation (4).
3. We estimated $k = \lambda_R(\mathrm{obs})/\lambda_R(\mathrm{iso})$, where $\lambda_R(\mathrm{obs})$ is the observed $\lambda_R$ at $R = 25''$ and $\lambda_R(\mathrm{iso})$ is $\lambda_R$ derived from our Jeans isotropic model at $R = 25''$. This ratio is analogous to the so-called Satoh's parameter (Satoh 1980), and it is an estimation of the tangential anisotropy. However, the interpretation of this ratio in real galaxies is not so simple, since this can be tied to the galaxy's inclination and the vertical anisotropy ($\delta$) (e.g., Cappellari et al. 2007).
4. $\lambda_R$ at $R_{1/2}$ was estimated as $\lambda_{R_{1/2}} = k\lambda_{R_{1/2}}(\mathrm{iso})$, where $\lambda_{R_{1/2}}(\mathrm{iso})$ is $\lambda_R$ at $R_{1/2}$ derived from our Jeans isotropic models. We recall that this is just an estimation of $\lambda_R$ at $R_{1/2}$, since this depends on *k* remaining constant within the galaxy, which may not be the case.
5. Finally, we calculated the ellipticity $\epsilon$ at $R_{1/2}$ from our surface brightness models used to derived our Jeans isotropic models, as was done in Cappellari et al. (2007), that is, by calculating the luminosity-weighted ellipticity within the inner $R = R_{1/2}$.

Correction to $R_{1/2}$ displaces the location of the galaxies mostly toward higher ellipticities and higher $\lambda_R$. Values for both the measured and corrected values are given in Table 7. In Figures 13 and 14, the measured and corrected values are connected by lines with the symbols located at the corrected values.

We compare the location of our galaxies in the $\lambda_R$–$\epsilon$ plane (Figure 13) with the location of simulated merger remnants from Jesseit et al. (2009) and Bois et al. (2011) in Figures 13 and 14, respectively. The simulations of Jesseit et al. (2009) are disk-disk mergers with mass ratios between 1:1 and 3:1, for both gasless ("dry") mergers and those with gas and star formation ("wet"). The simulations of Bois et al. (2011) are "wet" spiral-spiral mergers with mass ratios of either 3:1 or 6:1. The "progenitor" galaxies of Bois et al. (2011) are dynamically hotter than those in Jesseit et al. (2009) since they already include bulges with bulge-to-disk ratios corresponding to Sb and Sc galaxies. Thus, the Bois et al. (2011) progenitors represent galaxies that have likely already experienced gravitational disturbances. Simulations show that wet mergers produce more rounded remnants than dry mergers, especially in the low rotator region. All of our sample galaxies have gas, so comparisons with the wet mergers are most appropriate.

Our sample galaxies occupy three main regions in the $\lambda_R$–$\epsilon$ plane, an thus we refer to three groups: dynamically cold galaxies, dynamically lukewarm galaxies, and dynamically warm galaxies.

1. *Dynamically cold galaxies.* Two galaxies, NGC 4580 and NGC 4651, are consistent with the Jesseit et al. (2009) progenitor line and are well above the Bois et al. (2011) progenitors. In the case of NGC 4580, the stellar component of the galaxy looks undisturbed, so it probably has not been affected by any significant gravitational interaction. NGC 4651 displays a tidal tail and warped H I outer disk (Chung et al. 2009), suggesting an ongoing minor merger, but either its mass ratio must be very high or the merger is in an early phase, leading to a kinematically undisturbed inner disk.

2. *Dynamically lukewarm galaxies.* Most of our sample galaxies occupy a central band in the $\lambda_R$–$\epsilon$ plane, extending from ($\epsilon$, $\lambda_R$)≃(0.1,0.25) to (0.7,0.55). These lie well below the Jesseit et al. (2009) progenitor line and a bit below the Bois et al.

(2011) mean progenitor line. Some are in regions consistent with 3:1 or 6:1 merger remnants (NGC 4694, NGC 4450, NGC 4457, NGC 4429, and NGC 4698), although some with high ellipticities are beyond any of the merger regions (NGC 4293, NGC 4064, NGC 4569, and NGC 4606). Figure 13 shows that all of the high-ellipticity galaxies have weak bulges. At least some of these have bars. All of the galaxies in this group have likely experienced at least modest gravitational disturbances. While some could be 3:1 to 6:1 mergers, many could be minor mergers ($\geqslant$10:1) or tidal encounters, especially those with high ellipticity.

3. *Dynamically warm galaxy.* One galaxy in our sample, NGC 4424, is dynamically much warmer than any of the progenitors from either Jesseit et al. (2009) or Bois et al. (2011), and in a region consistent with a 3:1–6:1 merger remnant. Its rotational support is much less than any other sample galaxy, and it has been previously called a "low rotator" (Rubin et al. 1999), although it has enough rotation to qualify as a "fast rotator" as defined by Bois et al. (2011). Given its peculiar morphology and kinematics, NGC 4424 has been previously proposed as a merger remnant (Kenney et al. 1996; Cortés et al. 2006).

It is of interest to compare the dynamical state of the galaxies with their star formation classes. The only [N] galaxy in the sample is the dynamically coldest one. One of the three [T/N] galaxies, NGC 4580, is dynamically cold, providing further evidence that its truncated gas disk is due to ram pressure stripping rather than a gravitational interaction (Koopmann & Kenney 2004). The other two [T/N] galaxies, NGC 4457 and NGC 4569, are in the dynamically lukewarm band and may have experienced gravitational interactions in addition to unrelated ram pressure stripping events. For the [N] and [T/N] galaxies, the star formation classes are related to their dynamical state in the expected way.

Galaxies classified as [T/A] are all in the dynamically lukewarm band. All have bulges, and so the dynamically warm components may be bulges. Some of these may have had non-merging gravitational encounters, but others likely are the result of higher mass ratio mergers (mass ratios $\geqslant$ 1/6). This is consistent with the existence of kinematically distinct components in NGC 4450 and NGC 4429 and an orthogonally rotating core in NGC 4698. It has been unclear what has happened to these galaxies to give them [T/A] star formation distributions. Since they are all consistent with having gravitational disturbances, it is possible that the gravitational disturbances are responsible for the [T/A] distributions.

Galaxies classified as [T/C] are all in the dynamically lukewarm band, except for NGC 4424, which is dynamically hotter. [T/C] galaxies all have relatively high ellipticities. They all have small bulges, at least some have bars, and they happen to be viewed at a high inclination angle. It is notable that the dynamically warm or lukewarm component of these galaxies are not bulges, but disks. The high ellipticities are inconsistent with lower mass ratio mergers (mass ratios $\leqslant$1/6), so these galaxies have experienced either higher mass ratio mergers (mass ratios $\geqslant$1/6) or non-merging gravitational encounters. In terms of dynamical heating, the [T/C] galaxies are similar to the [T/A] galaxies but they have lower masses. The [T/A] galaxies have an average *H*-band absolute magnitude $\sim -23.5$, whereas the [T/C] galaxies have H $\sim -22$.

#### 7.1.2. Kinematic Peculiarities

*N*-body simulations (Jesseit et al. 2007) show that merger remnants display a high diversity in their 2D maps of various moments of the LOSVD. They display features such as low rotation, kinematical twists and misalignments, counter-rotating cores, $v$–$h_3$ correlations or anti-correlations, polar rings, low-$\sigma$ rings, and central $\sigma$ drops. Mergers are not the only gravitational interaction to cause dynamical heating and kinematics peculiarities. Recent chemodynamical numerical simulations (Bekki & Couch 2011) consider that slow tidal encounters of galaxies and group tides could be responsible for the transformation of spirals into S0s. These simulations show that the resulting galaxies display lower rotational velocities than their spiral progenitors ($V/\sigma \sim 1$), flat radial $\sigma$ profiles, or central dips in $\sigma$. High velocity encounters may also cause similar features. Here, we will refer to the sample galaxies that exhibit these telltale features.

Low rotation and flat $\sigma$ profiles. Flat $\sigma$ profiles and lower rotation amplitude ($V/\sigma \sim 1$) can be caused by either minor mergers (Bournaud et al. 2004; Jesseit et al. 2007)) or tidal encounters (Bekki & Couch 2011). Here, we have only one galaxy, NGC 4424, that has a rotation velocity below 30 km s$^{-1}$. Low rotation can be created in a 1:1 merger, but this is not likely for NGC 4424 since this galaxy exhibits an exponential light profile, which seems to contradict a 1:1 merger scenario. This kind of object with low rotation and an exponential light profile can be the result of higher mass ratio mergers (1:10–1:4; Bournaud et al. 2004). Flat $\sigma$ profiles and lower rotation amplitude are also observed in NGC 4064, NGC 4606, NGC 4694, and NGC 4698.

Kinematical misalignment and twist. In our galaxy sample, we do not find any galaxy with big kinematical misalignments ($\Psi > 30^\circ$), which are produced in 1:1 mergers. We do have one sample galaxy NGC 4293 with an intermediate amount of misalignment, $\Psi \leqslant 20^\circ$–$30^\circ$. In the case of 3:1 mergers, simulations (Jesseit et al. 2007) show that $\Psi \leqslant 20^\circ$. These are in better agreement with most of our galaxies. In the case of NGC 4651, $\Psi_{\rm outer} = 10^\circ \pm 4^\circ$ (Table 4), which is consistent with a minor merger. The most remarkable case of kinematical misalignment is NGC 4698 with its well-known orthogonally rotating core. This galaxy could be considered similar to polar ring galaxies, which can be formed by mergers with a dissipative component.

Counter-rotating core. We do not find any sample galaxy with this kind of feature, although the orthogonally rotating core in NGC 4698 clearly implicates an old merger, and a misaligned gas core in NGC 4424 (Cortés et al. 2006) strongly suggests a merger.

*$v$–$h_3$ correlation or anti-correlation.* Simulations show that a positive correlation between these quantities is created in the center of collisionless 3:1 remnants (Jesseit et al. 2007). The presence of gas suppresses the formation of this correlation, and leads instead to an anticorrelation between $v$–$h_3$. We see suggestions of such an anticorrelation in NGC 4429, NGC 4450, and NGC 4651.

*Double $\sigma$ peaks*. This feature has been seen in simulations of some equal-mass merger remnants with gas (Jesseit et al. 2007). In our sample, two galaxies display clearly off-axis double peaks, similar to what is seen in simulations. These are NGC 4424 and possibly NGC 4606. Both galaxies have truncated/compact H$\alpha$ morphologies with active star formation in the center. These feature suggest that these galaxies are indeed the result of mergers, but that such features are not unique to equal-mass mergers but can be present in non-equal mass mergers.

*Central $\sigma$ drops*. In simulations of both mergers (Jesseit et al. 2007) and tidal interactions (Bekki & Couch 2011) of

galaxies containing gas, the center often exhibits low $\sigma_{los}$ due to significant amounts of gas driven to the center which then forms stars. We found this in NGC 4429 and NGC 4694. NGC 4429 shows a clear $\sigma$ drop in the center, as well as other features (see Section 5.3) that suggest a cold circumnuclear stellar disk, which likely formed after most of the bulge component. NGC 4694 exhibits a small central dip in $\sigma$. The results of two-integral self consistent dynamical models (see Cortés et al. 2008) show a low $M/L \sim 1.0\, M_{\odot}/L_{\odot}$, together with its $B$–$V$ color (∼0.62), suggesting a recent starburst that could explain the $\sigma$ dip in the center.

### 7.2. ICM–ISM Stripping

While many Virgo cluster spiral galaxies show strong evidence for ongoing ram pressure stripping (Koopmann & Kenney 2004; Chung et al. 2007, 2009), we focused on galaxies with other peculiarities when selecting the present sample. Nonetheless, we included a couple of galaxies thought to be good examples of ongoing or past ram pressure stripping, NGC 4569 and NGC 4580. Two other galaxies in the sample, NGC 4351 and NGC 4457, may be experiencing ram pressure. We discuss these galaxies below. In addition, other galaxies in the sample may have experienced ram pressure stripping, in addition to gravitational encounters, since they are gas-poor, although we do not have evidence in our data for ongoing ram pressure interactions.

Active stripping is easier to identify in highly inclined galaxies, since a clear spatial separation of gas and stars can be seen (Kenney et al. 2004; Crowl et al. 2005; Abramson et al. 2011). In relatively face-on galaxies, a comparison of stellar and gas kinematics is a good way to identify ongoing ram pressure stripping. Ram pressure acts only on gas, so in a galaxy affected by ram pressure, the kinematics of the gas is disturbed but those of the older stars is not. If, however, star formation occurs in gas disturbed by ram pressure, then the stellar kinematics of the newly formed stars would be disturbed, and so the intensity-weighted stellar kinematics (including both young and old stars) could also be disturbed. Recent (e.g., Kronberger et al. 2008) combined $N$-body/hydrodynamic simulations have shown that ICM–ISM stripping has distinctive effects on the gas velocity fields, which become distorted. In the case face-on stripping, velocity fields look disturbed in the outer parts and undisturbed in the inner parts of the disk. As the inclination of the galaxy becomes more edge-on, the disturbance in the gas velocity field increases and it becomes asymmetric, with a mismatch between the gas kinematic center and the stellar disk center.

Some of our sample galaxies display features in their ionized gas velocity fields that may indicate ram pressure. NGC 4457 displays a stellar velocity field largely consistent with rotation, but an asymmetric ionized gas velocity field indicating non-circular gas motions. There is an apparent bending in the gas isovelocity contours on the southern side of the galaxy and gas velocities are 30–40 km s$^{-1}$ lower than the stellar velocities. This bending is also visible in the more detailed and extended map presented by Chemin et al. (2006). Also, its gas kinematic center does not seem to coincide with the optical center of the stellar disk, although the gas kinematic center is not well determined. Moreover, it presents a peculiar H$\alpha$ arm. ICM–ISM stripping simulations (e.g., Schulz & Struck 2001) show that this feature can be created in galaxies tilted with respect to the ICM wind. Overall, the disturbed gas kinematics and anomalous H$\alpha$ arm suggest active ram pressure stripping in NGC 4457.

NGC 4351 is lopsided, as the starlight in the central ∼30″ is significantly offset from the centroid of outer disk isophotes. Much of the central starlight arise from strong star formation with an irregular pattern. Otherwise, there are no obvious disturbances in the light distribution of the outer galaxy, which lacks star formation. The stellar velocity field is generally consistent with a rotation pattern (Figure 6), except that all of the isovelocity contours curve toward the SW. While not all of the features that deviate from a pure rotation pattern are real, the unusual curvature toward the SW may be real. A similar pattern is observed with high significance in both ionized gas velocity fields (Figure 6), as well as the H I velocity field (Chung et al. 2009). It remains unclear whether this apparently similar disturbance to the stellar and gas velocity fields is due to tidal interaction or ram pressure. While ram pressure does not affect stars, much of the stellar light we are measuring in this region could be from young stars that formed in gas disturbed by ram pressure. The H I distribution shows compressed contours to the NE and an extended, tail-like distribution to the SW (Chung et al. 2009). Similarly, the peak in ionized gas intensities is in the NE. All of these features may be consistent with ongoing ram pressure from the NE.

NGC 4580 has a sharply truncated gas disk within a relatively normal looking stellar disk. Its high $V/\sigma$ ratio confirms that the stellar disk is undisturbed. Its ionized gas velocity field looks symmetric and undistorted, indicating that strong ram pressure is not presently acting on the galaxy. The H$\alpha$ image of the galaxy shows a prominent star forming ring at the gas truncation radius (Koopmann & Kenney 2004). This could be a case of "annealing" (Schulz & Struck 2001) where some of the outer disk gas has lost angular momentum and forms a dense gas ring at the truncation radius which makes the remaining gas more resistant to stripping.

NGC 4569 may be the clearest case of ongoing ram pressure stripping in our sample, although our kinematic data do not show anything obviously related to this, since the telltale evidence is beyond the central field of view we studied. It has a sharply truncated gas disk within a relatively normal stellar disk, as well as an anomalous extraplanar arm of H I gas with star-forming regions that may be falling back into the galaxy. Vollmer et al. (2004) make the case that NGC 4569 is in a post-peak pressure phase after closest approach. The kinematic peculiarities we find in the central part of NGC 4569 reflect a nuclear outflow, which is not directly related to the ram pressure stripping.

## 8. PECULIAR CLUSTER GALAXIES AND ENVIRONMENTAL EFFECTS

The kinematic peculiarities of the sample galaxies are difficult to explain by internal mechanisms, and are presumably due to interactions within the cluster or circumcluster environment. Can these peculiarities be caused by a sole mechanism, or do we need more than one mechanism acting independently to explain them? In order to answer these questions, we focus on the probable scenarios for the galaxy peculiarities suggested by the stellar and ionized gas kinematics for all the sample galaxies.

In the Appendix, we present a detailed discussion on the kinematics of each sample galaxy, and in Table 8 we summarize the kinematic and morphological indicators of interactions for each galaxy and give our best guess for the types of interactions that the galaxies have experienced. All galaxies show evidence for ongoing, recent, or past interactions, and several galaxies show evidence for multiple interactions.

Two galaxies in our sample, NGC 4351 and NGC 4457, show possible evidence of ongoing ram pressure stripping based on our kinematic data. One galaxy that has been proposed as an

**Table 8**
Kinematic Disturbances and Evidence of Interaction

| Galaxy (1) | Morphological Features (2) | Kinematic Features (3) | Interaction (4) |
|---|---|---|---|
| NGC 4064 | Very strong stellar bar<br>disturbed dust morphology<br>truncated gas disk<br>[T/C] H$\alpha$ morphology | Very strong bar streaming motions<br>flat $\sigma$ profile | Gravitational interaction<br>ram pressure stripping |
| NGC 4293 | Outer stellar disk warped<br>disturbed dust lanes | Kinematic misalignment & twist | Gravitational interaction |
| NGC 4351 | Lopsided<br>H I compressed in NE & extended to SW | Curved isovelocity contours for star & gas<br>stars and gas misaligned | Ongoing ram pressure stripping? |
| NGC 4424 | Heart-shaped stellar body & shells<br>large H I tail<br>[T/C] H$\alpha$ morphology | Low $v/\sigma$ and flat $\sigma$ profile<br>off-center double $\sigma$ peaks<br>complex central gas motions | Recent intermediate-mass ratio merger<br>or close high-velocity collision<br>ram pressure stripping? |
| NGC 4429 | Central dust disk<br>cold circumnuclear stellar disk | Stellar $V$ rises rapidly in center then falls<br>pinched stellar isovelocity contours<br>$v$–$h_3$ anti-correlation<br>central $\sigma$ drop<br>LOSVD tail<br>misalignment between central disk and outer body | Old merger with gas infall to center |
| NGC 4450 | Cold circumnuclear stellar disk | Stellar & [O III] kinematic PA misalignment<br>$v$–$h_3$ anti-correlation<br>stellar V rises rapidly in center then falls<br>pinched stellar isovelocity contours<br>LOSVD tail | Gas accretion or minor merger |
| NGC 4457 | Peculiar 1 arm spiral in center | Curved gas isovelocity contours<br>gas velocities offset from stars by 30–40 km s$^{-1}$ | Ongoing ram pressure stripping? |
| NGC 4569 | Outer stellar disk warped<br>with respect to inner disk<br>truncated H I & H$\alpha$ disk<br>stripped outer disk<br>anomalous H I & H$\alpha$ extraplanar arm | Non-circular gas motions in center<br>due to nuclear outflow<br>misalignment between the optical<br>and kinematicsl major axes | Post-peak active ram pressure<br><br>gravitational interaction<br><br>nuclear gas outflow |
| NGC 4580 | Undisturbed stellar disk<br>truncated gas disk | High $v/\sigma$<br>undisturbed gas velocity field | Past ram pressure stripped outer disk |
| NGC 4606 | Disturbed stellar disk<br>disturbed dust lanes<br>[T/C] H$\alpha$ morphology | Flat velocity dispersion profile<br>off-center double $\sigma$-peaks | Intermediate mass ratio merger |
| NGC 4651 | Outer disk disturbed with shells<br>and tail in stars and H I<br>strong spiral arms at $R \sim 20''$ | Undisturbed stellar and gas kinematics<br>within the central 3 kpc<br>LOSVD tail at $R$ =10–20″<br>strong h$_3$ component with $v$–$h_3$ anti-correlation | Recent minor merger |
| NGC 4694 | Complex H I distribution with tail<br>extending to nearby dwarf<br>[T/C] H$\alpha$ morphology | Central $\sigma$ drop<br><br>Flat velocity dispersion profile<br>ionized gas kinematics disturbed | Recent merger/accretion |
| NGC 4698 | | Orthogonally rotating stellar bulge<br>flat velocity dispersion<br>stellar & gas kinematic PA misalignment | Old merger |

**Notes.** (1) Galaxy name; (2) relevant morphological features; (3) relevant kinematic features; (4) possible type of interaction.

example of past ram pressure stripping, NGC 4580 (Koopmann & Kenney 2004, Crowl et al. 2008), is confirmed in our kinematic data to be undisturbed and have a kinematically cold stellar disk, inconsistent with any past strong tidal interaction and perfectly consistent with the past ram pressure stripping scenario. All but one of our galaxies, NGC 4651, are very gas poor (Chung et al. 2009) and may have experienced gas stripping. Several of these galaxies show clear or possible evidence for ongoing or past stripping based on H I mapping (Chung et al. 2009), but not from our data.

Among the most intriguing objects in our sample are those four galaxies with truncated/compact H$\alpha$ morphologies. All have flat stellar velocity dispersion profiles. While NGC 4064, NGC 4424, and NGC 4606 have small bulges, all have much lower angular momentum parameters $\lambda_R$ than NGC 4580, a small-bulge galaxy with similar mass, indicating that their stellar disks have been heated. The only one of the four with a prominent bulge, NGC 4694, has a central dip in its velocity dispersion, suggesting a young circumnuclear stellar disk. These four galaxies have likely experienced gravitational interactions that have disturbed the stellar disks and driven gas to the central kiloparsec. NGC 4424, with the strongest kinematic and morphological disturbances, likely experienced a recent intermediate-mass ratio merger (Kenney et al. 1996; Cortés et al. 2006) or a close high-velocity collision with another galaxy. NGC 4694, with a complex H I distribution including a tail connecting to a nearby dwarf, clearly has experienced galaxy-galaxy tidal interaction, probably involving accretion

or a "partial merger", that is, the nearby dwarf was disrupted and part of it merged with NGC 4694. The detailed type of gravitational interaction is not as clear in NGC 4606 and NGC 4064, but their kinematic properties suggest intermediate-mass ratio mergers or close tidal encounters. These galaxies have probably also experienced ICM-ISM stripping since they are gas-poor, have very truncated H I and H$\alpha$ disks, and in the case of NGC 4424 an H I tail (Chung et al. 2007; Chung et al. 2009).

Several of the sample galaxies have kinematically distinct cores resulting from gas infall followed by star formation, and are likely signatures of accretion or mergers. NGC 4698, with its orthogonally rotating bulge, is clearly an old merger. NGC 4429, with its misaligned central stellar and dust disk, and the tail in its LOSVD, is likely an old merger due to the lack of gas observed in this galaxy, which probably was consumed in the subsequent star formation that formed the kinematically distinct core. NGC 4450, with the tail in its LOSVD and the kinematical misalignment between its central gas and stars, has likely experienced a recent minor merger. NGC 4694, with its central *sigma* drop and evidence for a young central stellar disk, plus the clearly disturbed H I, has likely experienced accretion or a partial merger with the dwarf galaxy it is currently interacting with. While it does not have a kinematically distinct core, the disturbed outer disk of NGC 4651 clearly indicates a recent minor merger, and the prominent tail in its stellar LOSVD at $r = 10''$–$20''$ suggests that the merger affected the inner galaxy. The old mergers could have happened before the galaxies entered the central part of the cluster. Among the galaxies with evidence for recent minor mergers, NGC 4651 is far behind the main cluster, and NGC 4694 and NGC 4450 have at 3D distances beyond, but not far from, the virial radius of the cluster.

Non-merging tidal encounters are likely responsible for the misaligned inner and outer disks in NGC 4569 and NGC 4293, as well as their central kinematic and morphological PA offsets. Fast tidal encounters are expected to be common in clusters, and may be responsible for some of the other kinematic peculiarities we have observed. Some features can be produced by either mergers or non-merging tidal encounters, and their origin can be hard to pinpoint without a fuller picture of the galaxies properties.

The fact that most (10/13) of our sample galaxies have signatures of some kind of gravitational interaction shows that they play important roles in driving cluster galaxy evolution. At least half of our sample galaxies show evidence for ICM-ISM stripping, a fraction that underestimates the general importance of gas stripping in clusters, since we chose mostly galaxies that exhibited features not consistent with simple ICM-ISM stripping. Thus, a significant fraction of cluster galaxies experience both gravitational interactions and ICM-ISM stripping.

## 9. SUMMARY

In this paper, we have studied the stellar and ionized gas kinematics of 13 bright peculiar Virgo Cluster galaxies to investigate the mechanisms responsible of their peculiarities. Our results are summarized as follows.

1. We present 2D maps of the stellar velocity $V$, and the stellar velocity dispersion $\sigma$ and the ionized gas velocity (H$\beta$ and/or [O III]) of the central $30'' \times 45''$ for galaxies in the sample. We show maps of the higher-order moments of the LOSVD $h_3$ and $h_4$ for the three galaxies with the highest signal-to-noise ratio. The stellar rotation curves and velocity dispersion radial profiles are determined for 13 galaxies, and the ionized gas rotation curves are determined for 6 galaxies. We show deviations from circular gas and stellar motions by subtracting models of circular motions from the data. We measure the kinematic position angles for the gas and stars, and compute the differences between the optical and kinematical major axes. We provide improved position angle and inclination values for some galaxies.
2. The stellar velocity fields in the centers of our sample galaxies are largely consistent with a rotational pattern, except for the strongly barred NGC 4064, and NGC 4698 which has an orthogonally rotating core.
3. NGC 4064 exhibits an S-type pattern in its stellar velocity field, and big differences between the optical and kinematical PA within the inner $10''$ due to strong non-circular motions caused by a central bar. The bar in NGC 4064 is unusually strong. It may be the strongest stellar bar observed to date in terms of deviations from circular motions for the stars. Large misalignments between the optical and kinematical major axes are also found in the stellar velocity field of NGC 4293, however, the presence of a bar in this galaxy is not clear.
4. Nine galaxies exhibit non-circular gas motions and/or systematic differences between the stellar and ionized gas kinematics. The causes of these anomalies are varied. There is a velocity gradient along the minor axis caused by a nuclear outflow in NGC 4569. There are large differences between the kinematic PA of the gas and stars in NGC 4698 and NGC 4450, even though both gas and stars have predominantly circular motions. We propose that this is caused by the gravitational interaction of the gas with the potential of the disk and orthogonally rotating bulge in NGC 4698, and recent gas accretion or a minor merger in NGC 4450. Two relatively face-on galaxies in our sample, NGC 4351 and NGC 4457, show possible evidence of ongoing ram pressure stripping based on distinctive curvatures in gas isovelocity contours consistent with ram pressure stripping.
5. Stellar velocity dispersion radial profiles exhibit a range of behaviors. Some galaxies have sharply decaying profiles, including NGC 4569, NGC 4651, and NGC 4450. Some have roughly flat profiles, such as NGC 4424, NGC 4606, NGC 4064, and NGC 4580. Others have more complex profiles with maximum values outside the center, including NGC 4698, NGC 4429, and NGC 4694. These galaxies have kinematically distinct cores. There is not a one-to-one correlation with a bulge-to-disk ratio, as there are galaxies with both large and small bulge-to-disk ratios that have relatively flat profiles.
6. The $V/\sigma$ ratios are bigger than unity where the exponential disk starts to dominate the light in most but not all of the galaxies. Galaxies such as NGC 4569, NGC 4580, and NGC 4651 are largely supported by rotation ($V/\sigma \geqslant 1$ at 0.05 $R_{25}$), but others such as NGC 4424, NGC 4429, and NGC 4698 have $V/\sigma < 1$ over the entire array, so they are supported by random motions as far out as we can measure.
7. Signatures of kinematically distinct stellar components have been found in several galaxies. Pinched isovelocity contours and analysis of the higher moments of the LOSVD ($h_3$, and $h_4$) reveal cold circumnuclear stellar disks in NGC 4429, and maybe in NGC 4450. In the case of NGC 4429, this disk has a mass one-fourth the mass of the bulge, and is misaligned with the outer disk, suggesting

a merger origin. NGC 4694 has a central $\sigma$ drop and evidence for a young central stellar disk that is probably related to an ongoing gravitational interaction. The stellar velocity field in NGC 4698 clearly reveals the existence of an orthogonally decoupled core (Bertola et al. 1999), undoubtedly due to an old merger. While it does not have a kinematically distinct core, the disturbed outer disk of NGC 4651 clearly indicates a recent minor merger, and the prominent tail in its stellar LOSVD at $r = 10$–$20''$ and an anticorrelation between $V$–$h_3$ suggests that the merger has affected the inner galaxy.

8. We have found no evidence of stellar counter-rotating components at least as big as 20% of the primary component. This indicates that disk galaxies with massive counter-rotating components are rare, and are only created under very special conditions.
9. We have computed for sample galaxies the angular momentum parameter $\lambda_R$, which describes the relative amounts of rotational and random stellar motions. Only two of our galaxies are consistent with being strongly dominated by rotation. Random stellar motions are dynamically important in most of our galaxies, indicating the importance of minor-to-intermediate-mass ratio mergers and gravitational interactions in establishing their dynamical states.
10. Several galaxies with small bulges and truncated/compact H$\alpha$ morphologies have low ratios of $V/\sigma$, flat radial $\sigma$ profiles, and values of $\lambda_R$ which indicate that their stars have been dynamically heated by gravitational interactions. This may include 3:1 or higher mass-ratio mergers, which are not as disruptive as 1:1 mergers, allowing the galaxies to retain their fast rotator characteristics and disk-like morphology but puffing up the disks. While ram pressure stripping may be partly responsible for the truncated gas disks in these truncated/compact galaxies, their properties cannot be fully explained by simple ram pressure stripping, and require gravitational interactions.
11. Comparison with simulations reveals that most (10/13) of our sample galaxies have signatures of some kind of gravitational interaction, showing that they play important roles in driving cluster galaxy evolution. At least half of the galaxies show evidence for ICM-ISM stripping, and several galaxies exhibit evidence for both. This implies that a significant fraction of cluster galaxies experience both gravitational interactions and ICM-ISM stripping.

The funding for this research has been provided by Fundación Andes, Chile; Fondap project grant 15010003, Chile. This work is part of the research on the Virgo Cluster and isolated spiral galaxies funded by NSF grant AST-0071251.

## APPENDIX

## DESCRIPTION OF INDIVIDUAL GALAXIES

In this section, we comment on the velocity and velocity dispersion fields for each galaxy, as well as some relevant background information from other sources. We also explain the peculiarities, H$\alpha$ type components, and features within the central $r \sim 25''$ region that we have mapped.

*NGC 4064.* NGC 4064 has a strong stellar bar that turns into very open spiral arms at larger radii. Star formation is very strong in the central ~1 kpc but virtually absent at larger radii. Disturbed dust lanes extend to ~3 kpc (Cortés et al. 2006). These features suggest some kind of gravitational interaction, plus a process that removes the outer disk gas.

The central stellar isovelocity contours indicate rotation plus non-circular motions. The S-type twisting in the isovelocity contours (Figure 6) is consistent with the pattern expected for a strong bar (Figure 2). Due to the strong bar-like streaming motions, the mean stellar kinematic major axis (PA = 129°; PA~ 100° for the central $r = 10''$) is very different from the photometric major axis of the inner galaxy, which reflects the bar (PA = 170°), and the photometric major axis of the outer galaxy (PA = 150°), which reflects the disk.

The stellar velocity dispersion field exhibits an off-center peak of 66 km s$^{-1}$, and an asymmetric shape with the line-widths greater on the NW side than the SE side. We think that this feature is real, although it is not clear whether it is a telltale signature of a minor merger or an uninteresting consequence of patchy dust extinction. Overall, the radial velocity dispersion profile is flat, which suggests some type of gravitational interaction.

The ionized gas emission is confined to the inner 10 arcsec and forms a bar-like structure (Figure 6) with star formation regions (traced by the H$\beta$ emission) along the major axis of the bar. The ionized gas (H$\beta$ and [O III]$\lambda$ 5007 emission) exhibits kinematic behavior roughly similar to the stars with barlike streaming motions (Figure 6). Strong CO emission in the central $10''$ shows even stronger barlike streaming motions (Cortés et al. 2006).

A more complete analysis can be found in Cortés et al. (2006). Its truncated H$\alpha$ and H I disks (Chung et al. 2009) suggest ICM–ISM stripping. Its location in the outskirts of the cluster ($d_{M87}$ = 2.9 mpc; Cortés et al. 2008) and recent quenching of the star-formation (just 425 myr; Crowl & Kenney 2008) suggest that this galaxy experienced the combined effect of a gravitational interaction and stripping at the outskirts of the cluster.

*NGC 4293.* The outer disk of NGC 4293 is tilted with respect to the inner disk, a clear signature of a gravitational interaction. Optical images shows two bright spiral arms ending at $r = 80''$ in a ring-like feature with PA = 75°. Beyond this, there is a sharp drop in surface brightness accompanied by a shift in PA that reaches PA = 66 ° at $r = 150''$.

The central stellar velocity field of NGC 4293 seems to be largely consistent with rotation. The perturbations in the isovelocity contours are likely due to the low signal-to-noise ratio of the spectra. However, the mean stellar kinematic position angle (PA = 42°) is very different from the inner disk optical PA ($\Psi \sim 35$ °), and also different from the outer optical position angle ($\Psi \sim 24$°; Table 4). Analysis of the Spitzer 3.6 $\mu$m image shows regular isophote shapes with PA = 77° in the central $r = 20''$ bulge-dominated region, so the inner stellar distribution is aligned with the rest of the galaxy inside $r = 80''$. Moreover, there is no clear photometric evidence of a bar, although we cannot rule out a bar extending largely along the line of sight. The stellar kinematic major and minor axes are largely perpendicular, and so there is also no clear kinematic evidence of a bar, although a map with higher S/N ratio will provide a better test of this. We have no other explanation for the large difference in kinematic and photometric PAs.

The stellar velocity dispersion shows a general increase toward the center. Not all of the structure apparent in the $\sigma$ map is real. Strong dust lanes near the center may affect the line shapes in some locations.

[O III] emission (Figure 6) was only detected in two regions separated by 10″. The scarcity of ionized gas emission made it impossible to obtain a reliable extended velocity field.

The misalignment between the kinematical and optical major axes, the disturbed dust lanes, and tilted outer stellar disk all strongly suggest a gravitational interaction.

*NGC 4351*. NGC 4351 is lopsided. The continuum light in the central ∼30″, where there is strong star formation with an irregular pattern, is significantly offset from the centroid of outer disk isophotes. Otherwise, there are no obvious disturbances in the light distribution of the outer galaxy, which lacks star formation. It has been unclear whether the peculiarities of this galaxy are due to ram pressure or a gravitational interaction.

The surface brightness of the stellar light in the center of NGC 4351 is fainter than most other sample galaxies, and so the signal-to-noise ratio of the spectra is lower (∼20 per pixel in the center).

The stellar velocity field is generally consistent with a rotation pattern (Figure 6), except that all of the isovelocity contours curve toward the SW. While not all of the features that deviate from a pure rotation pattern are real, the unusual curvature toward the SW may be real. A similar pattern is observed with high significance in both ionized gas velocity fields (Figure 6) as well as the H I velocity field (Chung et al. 2009). It remains unclear whether this apparently similar disturbance to the stellar and gas velocity fields is due to a tidal interaction or ram pressure. While ram pressure does not affect stars, much of the stellar light we are measuring in this region could be from young stars that formed in gas disturbed by ram pressure. The galaxy's large systemic velocity with respect to the cluster, and the large projected ICM density at its cluster location, suggest the action of ICM-ISM stripping.

The stellar velocity field displays a mean kinematical PA of 53° ± 8°, similar to the optical PA measured by us at $r = 100''$ and very different from the optical PA of 80° given by Koopmann et al. 2001. Ionized gas velocities (H$\beta$ and [O III]) exhibit a mean kinematical PA of about 62°, which is very similar to H I kinematical PA given by Chung et al. (2009).

The stellar velocity dispersion over the central field is constant within the errors at ∼25 km s$^{-1}$, the lowest value in the sample. It is difficult to measure dispersion variations in this galaxy due to both the low signal-to-noise ratio and the fact that the measured $\sigma$ (∼25 km s$^{-1}$) is of the order of the velocity resolution of the spectra.

*NGC 4424*. NGC 4424 is a strongly disturbed and highly peculiar galaxy. It has a heart-shaped stellar light distribution at intermediate radii and shell-like features in the outer disk, clearly indicating a merger or other major gravitational encounter (Kenney et al. 1996; Cortés et al. 2006). Star formation is very strong in the central ∼1 kpc, but virtually absent at larger radii. Disturbed dust lanes extend to ∼3 kpc (Cortés et al. 2006). It has an H I tail extending beyond the main body to the south (Chung et al. 2009), suggesting either ICM–ISM stripping or a collision with M49. The precise origin of this combination of peculiar features remains unclear.

The stellar velocity field is largely consistent with a rotation pattern. The small velocity range (400 km s$^{-1}$ $\leqslant V_{\rm los} \leqslant$ 470 km s$^{-1}$) within the inner 25″ shows the remarkably low velocity gradient exhibited by the stellar kinematics, which was previously observed in the ionized gas by Rubin et al. (1999).

The stellar velocity dispersion field is relatively flat but shows three modest peaks slightly offset from the major axis. One is located just north of the nucleus, and two others are nearly symmetrically located 10″ about the nucleus, roughly at the same location of the outermost luminous H II complexes.

Ionized gas intensity line maps show that H$\beta$ and [O III] emission are confined to two star forming regions roughly equidistant from the center (∼10″). The ionized gas velocity fields are completely different from the stellar velocity field, with isovelocity contours roughly perpendicular to the stellar velocity field. The amount of non-circular motions in the ionized gas velocity fields made it impossible to obtain reliable gas rotation curves.

*NGC 4429*. NGC 4429 is an S0 galaxy notable for a very regular dust disk that extends to 10″. It has no other known peculiarity. Emission lines were not detected.

The stellar velocity field has a well-defined spider diagram, consistent with a rotation pattern (Figure 6) except for minor variations along the minor axis to the north. The isovelocity contours are pinched in the inner 5″ due to a large central velocity gradient. Two peaks symmetrically located around the nucleus at 10″ suggest a rapidly rotating second stellar component associated with the dust disk. Similar features have also been observed in other early-type disk galaxies such as NGC 4526, NGC 4570, and NGC 4621 (Emsellem et al. 2004).

The stellar velocity dispersion field exhibits two peaks offset from the center and a dip in the central part probably due to a cold central stellar disk, as in NGC 7332 (Falcón-Barroso et al. 2004) and NGC 4526 (Emsellem et al. 2004), plus the effects of dust extinction on the line profiles.

The cold stellar disk embedded with a big bulge could be the result of gas falling to the center, which can happen due to the presence of gas in a merger (Jesseit et al. 2007). Since NGC 4429 presently has no gas and no signs of any recent disturbance, we think the merger must have happened a long time ago.

*NGC 4450*. NGC 4450 is a large spiral with an anemic star forming disk that appears to be truncated in the outer galaxy at $r = 60''$ (Koopmann et al. 2001). The central region that we mapped includes a bulge and the inner part of a large-scale stellar bar with a PA ∼ 10° that extends to $r \sim 50''$.

The stellar velocity field shows fairly regular kinematics, mostly consistent with a rotation pattern. A considerable pinching in the isovelocity contours in the inner 3″ indicates a large central velocity gradient. The two plateaus in the stellar velocity field symmetrically located at $r \sim 5''$ are similar to the two peaks in NGC 4429 and suggest the presence of a secondary rapidly rotating component. The mean central stellar kinematic position angle differs by −12° ± 5° with respect to the outer optical PA.

The stellar velocity dispersion is centrally peaked and relatively asymmetric.

H$\beta$ emission is very weak and is confined to only a few fibers within the array. [O III] λ5007 emission is brighter and more extended (Figure 6). The [O III] velocity field seems to be dominated by rotation, but with a position angle offset by 30° with respect to the central stellar velocity field, indicating significant non-circular motions or possibly a central gas disk tilted with respect to the stellar disk. If it is a tilted gas disk, then it would probably not survive long due to gravitational torques and gas dissipation, so we think this gas was recently acquired.

*NGC 4457*. This nearly face-on galaxy has significant H I and star formation in the central 30″, and virtually nothing beyond. The inner ISM-rich part of the galaxy is dominated by one peculiar strong spiral arm.

The stellar velocity field displays a pattern consistent with rotation. The stellar kinematic PA is 70° and probably corresponds to the line of nodes of the galaxy.

As in NGC 4429 and NGC 4450, there are pinched isovelocity contours within the inner 5″ and two peaks in the stellar velocity located at around 5″.

The stellar velocity dispersion is relatively constant over the central field, although it has a modest peak in the very center. The azimuthally averaged sigma profile shows a possible secondary peak at $r = 10''$, although the irregular pattern in the sigma map and the low signal-to-noise ratio make this uncertain.

The ionized gas intensity maps (Figure 6) display emission near the nucleus and on the spiral arms. The ionized gas velocity fields show a dominant rotational component, but also large non-circular motions indicating some type of disturbance. The isovelocity contours appear to be curved systematically toward the west, although our map is sparse. However, this curvature is also present in the more extended and detailed Hα velocity field presented in Chemin et al. (2006). Both maps show a strongly blueshifted region close to the core of the galaxy. The kinematic PA of the ionized gas is close to that of the stars, but the Hβ and [O III] velocities are systematically lower than the stellar velocities by 30–40 km s$^{-1}$. Along the stellar kinematic minor axis, ionized gas velocities show big differences with respect to the stars, becoming systematically redshifted on both sides of the nucleus, indicating non-circular motions in the gas. This gas isovelocity pattern resembles that observed in NGC 4351. We were unable to obtain reliable rotation curves for the gas due to the amount of non-circular motions in the velocity fields.

The gas kinematics seem consistent with ongoing ICM-ISM stripping. In fact, the presence of a peculiar Hα arm could also be explained as the result of ICM wind (Schulz & Struck 2001).

*NGC 4469*. This large spiral has an H I and star-forming disk truncated at $r \sim 90''$, and an unusual extraplanar arm of gas and star formation due to ram pressure stripping. Its outer stellar disk ($r \sim 170''$–$270''$; PA $\sim 25°$) is slightly twisted with respect to its inner disk ($r \sim 70$–$140''$; PA $\sim 20°$). It has a bright nucleus, is a known LINER (e.g., Keel 1996), and has a nuclear outflow.

The central stellar velocity field is largely consistent with a rotation pattern, although velocities on the NW side of the minor axis are systematically blueshifted by a few km s$^{-1}$ with respect to pure rotation, perhaps due to the effects of the prominent dust lanes present in this galaxy (Figure 2) since they are strong on the NW side. In the central 10″, there are other apparent deviations from pure rotation without any clear pattern, and these might also be caused by the effects of dust. This galaxy exhibits a small difference between the mean stellar kinematic PA (32°) and the optical photometric PA (23°)(ΔPA $\sim 9°$), which could be the result of a tidal interaction.

The stellar velocity dispersion has a strong central peak and drops sharply with radius. The dropoff is steeper along the minor axis than the major axis, which is a reflection of the highly inclined viewing angle.

The ionized gas intensity maps (Figure 6) show that both Hβ and [O III] emissions are associated with the central starburst. Hβ, but not [O III], is also located to the NW where the star formation ring is located, and [O III], but not Hβ, is detected south of the nucleus.

The gas velocity fields are very disturbed, indicating significant non-circular motions. Along the minor axis, the gas velocities reach a maximum value of −290 km s$^{-1}$ with a velocity amplitude of about 70 km s$^{-1}$. These are likely due to the nuclear outflow known to exist from the extended radio and Hα features along the minor axis (Chyży et al. 2006).

We could not obtain ionized gas rotation curves due to the amount of large non-circular motions in the gas.

*NGC 4580*. NGC 4580 has H I and Hα emission only out to a radius of 26″, where there is a prominent star formation ring. The outer disk has stellar spiral arms.

The stellar velocity field displays a nice spider diagram consistent with a rotation pattern (Figure 6), and shows no significant non-circular motions. The central stellar kinematic major axis is very close to the photometric major axis.

The stellar velocity dispersion is relatively constant over the central field, and the irregular features in the dispersion map are probably not real.

The ionized gas intensity maps exhibit Hβ emission over much of the array (Figure 6) with the strongest emission associated with the star formation ring. The [O III] emission is poorly correlated with the Hβ emission with peaks in regions where Hβ is weak.

The Hβ velocity field shows an overall pattern of rotation with the same kinematic position angle as the stars. The gas isovelocity contours show wiggles indicating localized non-circular motions that may be associated with the star forming ring.

The undisturbed, stellar, and ionized gas kinematics indicate that there are no signatures of gravitational interaction or ongoing strong ICM-ISM stripping. The presence of a truncated Hα disk with stellar spiral arms in a gas-poor outer disk indicates that ICM-ISM stripping probably took place within the last Gyr (475 Myrs ago; Crowl & Kenney 2008).

*NGC 4606*. NGC 4606 has a truncated/compact Hα morphology, meaning that there is strong star formation in the central 1 kpc but none beyond. It has a disturbed stellar body with non-elliptical isophotes, indicating a strong gravitational encounter. It is an apparent pair with the spiral NGC 4607, separated by 17 kpc and 600 km s$^{-1}$.

The stellar velocity field is dominated by a rotation pattern (Figure 6) but some minor distortions are present. The stellar kinematical major axis PA = 39° in the inner 20″ agrees well with the PA = 44° measured from the optical photometry of the outer galaxy.

The stellar velocity dispersion is essentially constant with a value of 49 ± 3 km s$^{-1}$. Two apparent peaks in $\sigma$ are located about 12″ north and south from the center, although the significance of these features is low. Simulations show that flat velocity dispersion profiles (Bendo & Barnes 2000) and off-axis $\sigma$ peaks (Jesseit et al. 2007) can be produced in mergers with mass ratios ∼3:1.

The ionized gas emission is confined to the inner 10″ (Figure 6). The strongest emission arises from an elongated bar-like string of luminous H II complexes, similar to those in the other truncated/compact galaxies, NGC 4064 and NGC 4424. There is a westward extension in [O III] emission with no Hβ counterpart, along the minor axis. The Hβ velocity field exhibits a gradient along the major axis that could be consistent with rotation. Ionized gas emission is too scarce to derive further conclusions.

*NGC 4651*. Over most of the optical disk, NGC 4651 looks like a relatively normal spiral galaxy, but the outer parts are strongly disturbed with shell-like features and a peculiar straight tail (Chung et al. 2009), probably due to a minor merger.

The central stellar velocity field is well ordered with a pattern strongly dominated by rotation. The stellar kinematical major

axis PA = 82° in the inner 20″ agrees well with the PA = 80° measured from both the optical photometry and the H I velocity field of Chung et al. (2009) at intermediate radii ($r \sim$ 30–90″). While to align the DensePak array we used PA = 71° from the optical photometric major axis measured at $R_{25}$ (Koopmann et al. 2001), this PA is characteristic of the outer galaxy ($r > 100''$) where the galaxy appears to be disturbed.

The stellar velocity dispersion is centrally peaked and decreases strongly with radius. A clear elongation is detected with high significance along the major axis of the galaxy. This feature is likely associated with a deviation from the Gaussian distribution in the LOSVD, which contains a strong $h_3$ component (see Section 5.3).

This is just inside the radius of the unusually bright, tightly wound spiral arms at $r \sim 20''$, suggesting that both might be related to the minor merger.

The H$\beta$ intensity map exhibits emission from star formation in the tightly wound spiral arms at $r \sim 20''$ (Figure 6), but very weak emission from the center. The [O III] intensity map shows strong emission over the nucleus and the spiral arms. Both ionized gas velocity fields appear largely similar to the stellar velocity field beyond the central 10″, although both H$\beta$ and [O III] maps show wiggles in the isovelocity contours that could be associated with spiral arms. Within the inner 10″, the [O III] map exhibits a twisting in the isovelocity contours indicating non-circular motions in this gas.

*NGC 4694.* NGC 4694 has strong emission from the nuclear region due to star formation and/or an active galactic nucleus, and otherwise it has weak star formation in the central kiloparsec, and none beyond. A disturbed complex of H I extends across the minor axis to the nearby faint galaxy VCC 2062, indicating some kind of gravitational interaction, perhaps a minor merger or gas accretion event (Chung et al. 2009).

The stellar velocity field is largely consistent with a rotation pattern, although it shows some modest apparent deviations from circular motions that have low significance. Along the minor axis (PA = 56°), the stellar velocities do not display any gradient. The PA of the stellar kinematical major axis in the center agrees well with the PA measured from optical photometry in the outer disk.

The stellar velocity dispersion is practically flat with a small dip in the center. Some of the apparent variations exhibited in the outer parts are likely artifacts due to a low signal-to-noise ratio.

The ionized gas intensity maps show emission within the central 10″. The nucleus is relatively strong with fainter features extending to the NW and SW (Figure 6). The ionized gas velocity fields appear disturbed. Along the major axis, ionized gas velocities are systematically lower by 25 km s$^{-1}$ than the stars, and in places show large velocity gradients.

*NGC 4698.* This remarkable galaxy NGC 4698 has a bulge that rotates orthogonally with respect to the disk (Bertola et al. 1999). The disk appears to be undisturbed, suggesting that this galaxy is the product of an ancient merger.

The stellar velocity field shows at least two distinct kinematical components (Figure 6). The inner 10″ exhibits S-shaped isovelocity contours near the minor axis due to the orthogonally rotating core. The effect is less evident that in previously published data (Bertola et al. 1999), due to the smoothing effect introduced by the width of the fibers. In the outer 10″, the velocity field is consistent with a rotation pattern in most respects, except that the isovelocity contours are concave. These concave contours mean that the line-of-sight velocity increases as we move outward from the major axis, which is probably due to the effect of the orthogonally rotating bulge. This galaxy exhibits almost no stellar rotation within the inner 10″. Beyond the inner 10″, the LOS stellar velocities rise dramatically, due to the increasing influence of the stellar disk.

The stellar velocity dispersion has a modest peak at the center, but otherwise remains flat along the major and minor axes.

H$\beta$ emission was not detected. On the contrary, [O III] emission is very strong in the center and detected over the entire array (Figure 6). The [O III] velocity field is well ordered but very different from the stellar velocity field.

The pattern seems to be largely consistent with rotation, although with a PA that changes with increasing radius from 120° at the center to 150° at 25″. (In order to produce the [O III] rotation curve in Figure 8, we used rings with different PAs.) In the inner $r \sim 5''$, the [O III] kinematic PA is roughly perpendicular to the local stellar kinematic PA. At $r \sim 25''$, the PAs are offset by ∼20°. We suspect that the gas distribution is non-planar, as the equilibrium plane of the gas is expected to gradually change from larger radii, where the outer disk dominates the gravitational potential, to smaller radii, where the orthogonally rotating bulge dominates the potential.

## REFERENCES


Abraham, R. G., Valdes, F., Yee, H. K. C., & van der Bergh, S. 1994, ApJ, 432, 75
Abramson, A., Kenney, J. D. P., Crowl, H. H., et al. 2011, AJ, 141, 164
Athanassoula, E. 1992, MNRAS, 259, 345
Barbier–Brossat, M., & Figon, P. 2000, A&AS, 142, 217
Barden, S. C., Sawyer, D. G., & Honeycutt, R. K. 1998, Proc. SPIE, 3355, 892
Begeman, K. G. 1989, A&A, 223, 47
Bekki, K. 1999, ApJL, 510, L15
Bekki, K., & Couch, W. J. 2011, MNRAS, 415, 1783
Bendo, G. J., & Barnes, J. E. 2000, MNRAS, 316, 315
Bertola, F., Corsini, E. M., Vega Beltrán, J. C., et al. 1999, ApJL, 519, L127
Bingelli, B., Tammann, G. A., & Sandage, A. 1987, AJ, 94, 241 (BST)
Böhringer, H., Briel, U. G., Schwarz, R. A., et al. 1994, Natur, 368, 828
Bois, M., Emsellem, E., Bournaud, F., et al. 2011, MNRAS, 416, 1654
Bottema, R. 1993, A&A, 275, 16
Bournaud, F., Combes, F., & Jog, C. J. 2004, A&A, 418, L27
Butcher, H., & Oemler, A., Jr. 1978, ApJ, 219, 18
Butcher, H., & Oemler, A., Jr. 1984, ApJ, 285, 426
Cappellari, M., & Copin, Y. 2003, MNRAS, 342, 345
Cappellari, M., & Emsellem, E. 2004, PASP, 116, 138
Cappellari, M., Emsellem, E., Bacon, R., et al. 2007, MNRAS, 379, 418
Cen, R. 2014, ApJ, 781, 38
Chemin, L., Balkowski, C., Cayatte, V., et al. 2006, MNRAS, 366, 812
Chung, A., van Gorkom, J. H., Kenney, J. D. P., Crowl, H., & Vollmer, B. 2009, AJ, 138, 1741
Chung, A., van Gorkom, J. H., Kenney, J. D. P., & Vollmer, B. 2007, ApJL, 659, L115
Chyży, K. T., Soida, M., Bomans, D. J., et al. 2006, A&A, 447, 465
Coccato, L., Corsini, E. M., Pizella, A., & Bertola, F. 2005, A&A, 440, 107
Cortés, J. R., Kenney, J. D. P., & Hardy, E. 2006, AJ, 131, 747
Cortés, J. R., Kenney, J. D. P., & Hardy, E. 2008, ApJ, 683, 78
Crowl, H. H., & Kenney, J. D. P. 2008, AJ, 136, 1623
Crowl, H. H., Kenney, J. D. P., van Gorkom, J. H., & Vollmer, B. 2005, AJ, 130, 65
de Vaucouleurs, G., de Vaucouleurs, A., Corwin, H. G., et al. 1991, Third Reference Catalog of Bright Galaxies (New York: Springer) (RC3)
Dressler, A. 1980, ApJ, 236, 351
Dressler, A., Oemler, A., Jr., Couch, W. J., et al. 1997, ApJ, 490, 577
Emsellem, E., Cappellari, M., Krajnović, D., et al. 2011, MNRAS, 414, 888
Emsellem, E., Cappellari, M., Krajnović, D., et al. 2007, MNRAS, 379, 401
Emsellem, E., Cappellari, M., Peletier, R. F., et al. 2004, MNRAS, 352, 721
Falcón–Barroso, J., Bacon, R., Bureau, M., et al. 2006, MNRAS, 369, 529
Falcón–Barroso, J., Peletier, R. F., Emsellem, E., et al. 2004, MNRAS, 350, 35
Fillmore, J. A., Boroson, T. A., & Dressler, A. 1986, ApJ, 302, 208
Gavazzi, G., Boselli, A., Scodeggio, M., Pierini, D., & Belsole, E. 1999, MNRAS, 304, 595
Gavazzi, G., Pierini, D., & Boselli, A. 1996, A&A, 312, 397

Georgantopoulos, I., & Sezas, A. 2003, ApJ, 594, 704
Gunn, J. E., & Gott, J. R. 1972, ApJ, 176, 1
Héraudeau, Ph., Simien, F., Maubon, G., & Prugniel, Ph. 1999, A&AS, 136, 509
Hernquist, L. 1992, ApJ, 400, 460
Ho, L. C., Rudnick, G., Rix., H.-W., et al. 2000, ApJ, 541, 120
Jarrett, T. H., Chester, T., Cutri, R., Schneider, S. E., & Huchra, J. P. 2003, AJ, 125, 525
Jesseit, R., Cappellari, M., Naab, T., Emsellem, E., & Burkert, A. 2009, MNRAS, 397, 1202
Jesseit, R., Naab, T., Peletier, R., & Burkert, A. 2007, MNRAS, 376, 997
Kannappan, S. J., & Fabricant, D. G. 2001, AJ, 121, 140
Keel, W. C. 1996, PASP, 108, 917
Kenney, J. D. P., Koopmann, R. A., Rubin, V. C., & Young, J. S. 1996, AJ, 111, 152
Koopmann, R. A., & Kenney, J. D. P. 1998, ApJL, 497, L75
Koopmann, R. A., & Kenney, J. D. P. 2004, ApJ, 613, 866
Koopmann, R. A., Kenney, J. D. P., & Young, J. 2001, ApJS, 135, 125
Kormendy, J., & Bender, R. 2012, ApJS, 198, 2
Kronberger, T., Kapferer, W., Schindler, S., & Ziegler, B. L. 2007, A&A, 473, 761
Kronberger, T., Kapferer, W., Unterguggenberger, S., Schindler, S., & Ziegler, B. L. 2008, A&A, 483, 783
Larson, R. B., Tinsley, B. M., & Cadwell, C. N. 1980, ApJ, 237, 692
Mazzalay, X., Maciejewski, W., Erwin, P., et al. 2014, MNRAS, 438, 2036
Mei, S., Blakeslee, J. P., Côté, P., et al. 2007, ApJ, 655, 144
Moore, B., Katz, N., Lake, G., Dressler, A., & Oemler, A. 1996, Natur, 379, 613
Munari, U., Henden, A., Belligoli, R., et al. 2013, NA, 20, 30
Nulsen, P. E. J. 1982, MNRAS, 198, 1007
Poggianti, B. M., Fasano, G., Bettoni, D., et al. 2009, ApJL, 697, L137
Poggianti, B. M., Smail, I., Dressler, A., et al. 1999, ApJ, 518, 576
Rix, H.-W., Franx, M., Fisher, D., & Illingworth, G. 1992, ApJ, 400, 5
Rix, H.-W., & White, S. D. M. 1992, MNRAS, 253, 389
Rubin, V. C., Graham, J. H., & Kenney, J. D. P. 1992, ApJL, 394, L9
Rubin, V. C., Waterman, A. H., & Kenney, J. D. P. 1999, AJ, 118, 236
Rudnick, G., Rix, H.-W., & Kennicutt, R. C., Jr. 2000, ApJ, 538, 569
Sandage, A., & Bedke, J. 1994, The Carnegie Atlas of Galaxies (Washington, DC: Carnegie)
Sandage, A., & Tammann, G. A. 1987, A Revised Shapley-Ames Catalog of Bright Galaxies, (Washington, DC: Carnegie) (RS)
Satoh, C. 1980, PASJ, 32, 41
Schulz, S., & Struck, C. 2001, MNRAS, 328, 185
Scorza, C., & Bender, R. 1995, A&A, 293, 20
Simien, F., & Prugniel, Ph. 1997, A&AS, 126, 15
Solanes, J. M., Sanchis, T., Salvador-Solé, R., Giovanelli, R., & Haynes, M. P. 2002, AJ, 124, 2440
Toomre, A., & Toomre, J. 1972, ApJ, 178, 623
van Driel, W., & van Woerden, H. 1989, A&A, 225, 317
van Gorkom, J. H. 2004, in Cluster of Galaxies: Probes of Cosmological Structure and Galaxy Evolution, ed. J. S. Mulchaey, A. Dressler, & A. Oemler (Cambridge: Cambridge Univ. Press), 305
Vauterin, P., & Dejonghe, H. 1997, MNRAS, 286, 812
Vega-Beltrán, J. C., Pizella, A., Corsini, E. M., et al. 2001, A&A, 374, 394
Veilleux, S., Shopbell, P. L., & Miller, S. T. 2001, AJ, 121, 198
Vollmer, B., Balkowski, C., Cayatte, V., van Driel, W., & Huchtmeier, W. 2004, A&A, 419, 35
Vollmer, B., Cayatte, V., Balkowski, C., & Duschl, W. J. 2001, ApJ, 561, 708